Journal of the Mechanics and Physics of Solids 138 (2020) 103893

Contents lists available at ScienceDirect

Journal of the Mechanics and Physics of Solids

journal homepage: www.elsevier.com/locate/jmps

A constitutive model of microfiber reinforced anisotropic hydrogels: With applications to wood-based hydrogels

Jian Cheng[a], Zheng Jia[b,*], Teng Li[a,*]

[a] Department of Mechanical Engineering, University of Maryland, College Park, Maryland, 20742, USA
[b] Key Laboratory of Soft Machines and Smart Devices of Zhejiang Province, Center for X-Mechanics, Department of Engineering Mechanics, Zhejiang University, Hangzhou, 310027, China

ARTICLE INFO

Article history:
Received 24 October 2019
Revised 16 January 2020
Accepted 28 January 2020
Available online 8 February 2020

Keywords:
Constitutive model
Anisotropic hydrogels
Microfiber-reinforced hydrogels
Wood-based hydrogels
Actuators

ABSTRACT

Recent years have witnessed a surging growth in developing anisotropic hydrogels. Particularly, a new type of microfiber-based anisotropic hydrogel has emerged by transforming nature's existing anisotropic soft materials into hydrogels. For example, wood-based hydrogels feature crosslinked networks serving as the matrix with stiffer micro-sized cellulose bundles as the reinforcement. These anisotropic hydrogels resemble the anisotropic microstructure of living organisms and hold promise for broad applications. Despite its promising outlook, well-formulated mechanical models remain unavailable for microfiber-reinforced anisotropic hydrogels. The existing constitutive models are limited to simplified fiber configurations, making them only suitable for anisotropic hydrogels with macro-sized fibers but inadequate to capture complex microfiber distribution. Moreover, in sharp contrast to the nonlinear behavior of cellulose microfibers in wood-based hydrogels, fibers in most existing models are usually linear-elastic. Aiming to address this deficiency, we have established a micromechanical constitutive model suitable for microfiber-reinforced anisotropic hydrogels. Fiber distributions are included in the proposed constitutive model, which makes possible the investigation of various fiber reinforcement configurations. We explore several important anisotropic mechanical behaviors of the microfiber-reinforced hydrogel, including the anisotropic swelling, and anisotropic stress-strain relation in uniaxial tensile loading. More importantly, we apply the present model to analyze the performance of a humidity-sensitive actuator based on a bilayer of wood-based hydrogel and polyimide. The proposed constitutive model may promote theoretical understandings on the mechanical properties of anisotropic hydrogels and anisotropic-hydrogels-based soft machines.

1. Introduction

Hydrogel has emerged as one of the most promising bio-mimicking materials due to its ultrahigh water content (Ahmed, 2015), responsiveness to stimuli (Ionov, 2014), and extraordinary bio-compatibility (Billiet et al., 2012). Inspired by nature's broad lore of deformation mechanisms, in fields such as soft actuators and soft robots, researchers have devoted great attention to reproducing morphology transforming schemes of living organisms using man-made hydrogels.

* Corresponding authors.
E-mail addresses: zheng.jia@zju.edu.cn (Z. Jia), lit@umd.edu (T. Li).

https://doi.org/10.1016/j.jmps.2020.103893
0022-5096/

Even though the living organisms are often characterized by a highly hierarchical, directional and anisotropic microscopic structure (Burgert and Fratzl, 2009; Calvert, 2009; Fratzl et al., 2008), in sharp contrast, their artificial counterpart, hydrogel, usually possesses an isotropic architecture, owing to the conventional polymerization process (Sano et al., 2018). However, anisotropic structures have an enabling role in the performance of physiological functions: muscle depends on the uniaxial contractions of the muscle fibers to act; cartilage relies on the anisotropic structure of collagens to provide lubricating intraosseous support; and the directional mass transportation inside plant vascular bundles is realized by the highly aligned cellulose fibers.

To bridge this gap, an array of approaches to endowing hydrogel with oriented microstructures have been developed within the past decade to mimic nature's anisotropic soft matters. These efforts can be categorized into three distinctive types (Sano et al., 2018): (i) Hybrid hydrogel with interacting micro/nano-fillers (Kim et al., 2015; Liu et al., 2015a; Palagi et al., 2016); (ii) hydrogel with aligned microporous structures resulting from the directional crystallization of solvent (De France et al., 2018; Liu et al., 2016a); (iii) Hydrogel with aligned reinforcement fibers or secondary network (Gladman et al., 2016; Lin et al., 2016). These efforts have unleashed a rapid growth in anisotropic hydrogels with enhanced mechanical performances owing to their intrinsic microscopic structures mimicking living organisms. In this regard, the novelty and significance of anisotropic hydrogels have been demonstrated in various applications such as bio-mimicking actuation. For example, Kim et al. developed an anisotropic hydrogel with electrostatically interacting nanofillers and demonstrated its application in a unidirectional progressing biped soft robot (Kim et al., 2015). Gladman et al. invented a complicated shape transform achieved by a 4D-printed anisotropic hydrogel with locally oriented cellulose fibrils (Gladman et al., 2016). The deformation behavior of the hydrogel can be readily modulated by tuning the fiber alignment via the printing process. As a common strategy shared by these examples, the anisotropy is imparted to the otherwise originally isotropic hydrogel matrix via microstructural modifications, so that hydrogels are made anisotropic.

More recently, a new strategy is demonstrated to construct anisotropic hydrogel by directly reorganizing the microstructure of nature's existing anisotropic materials. The structures of living organisms are naturally anisotropic (bio-tissue, wood, etc.). Therefore, anisotropic hydrogels can be derived by transforming nature's anisotropic materials into hydrogels. For example, natural wood can be chemically processed to expose the hydrophilic cellulose nanofibers (CNF) originally bundled within the wood cell walls (Kuang et al., 2019), which form a cross-linked cellulose hydrogel once in contact with water. The cross-link can be made either physically by promoting the hydrogen bond percolating network (Kuang et al., 2019), or chemically by further functionalizing the cellulose fiber precursors (Ye et al., 2018). The cellulose fibers can also be mixed with polymeric hydrogel precursor to form cellulose-fiber-reinforced hydrogels (Kong et al., 2018). The abovementioned aggregates of cellulose fibers, water, and crosslinked hydrophilic networks can be termed as wood-based hydrogels. In these wood-based hydrogels, CNF bundles (a.k.a., cellulose microfibers) serve as the reinforcement phase, providing stiffness and mechanical strength; the hydrophilic networks formed by crosslinked polymer chains (Kong et al., 2018) or cellulose nanofibers tethered to the surface of CNF bundles (Kuang et al., 2019) absorb and retain water molecules. For applications of wood-based hydrogels, Kuang et al. (Kuang et al., 2019) demonstrated a cellulose-nanofiber-based anisotropic actuator driven by humidity change. Benefiting from its anisotropic microstructure, the actuator outperforms other designs of the same kind with isotropic structures in both response time and lifting weight ratio. Furthermore, wood-based hydrogels also inherit the excellent mechanical properties of wood. According to Kong et al. (Kong et al., 2018), the wood-based hydrogel exhibits an ultimate tensile strength 500 times of the traditional polyacrylamide hydrogel.

The emerging anisotropic hydrogels and their broad applications have motivated recent development of the constitutive models for anisotropic fibrous hydrogels. Following the approach by Holzapfel (Holzapfel, 2000), Pan and Zhong (Pan and Zhong, 2014) proposed a constitutive model to understand the mechanical degradation due to moisture absorption of unidirectional fiber-reinforced composites. Nardinocchi et al. (Nardinocchi et al., 2015) presented an enhanced version of the Flory-Rehner free energy (Flory and Rehner, 1943) by accounting for the reinforcement effect of aligned fibers, to investigate the anisotropic response of fiber-reinforced hydrogels. Liu et al. (Liu et al., 2016b, 2015b) implemented the above constitutive model into the finite element framework to model the anisotropic swelling behaviors of fibrous hydrogels. Liu et al. (Liu et al., 2018) also conducted direct numerical simulations to explore the anisotropic contraction of fiber-reinforced hydrogels by resorting to the finite element method. Bosnjak et al. (Bosnjak et al., 2019) enriched the continuum-level constitutive model for fiber-reinforced polymeric gels by further taking into account the anisotropic diffusion of water. In these models, fibers are taken to be macro-fibers that feature a linear-elastic response, in sharp contrast to the nonlinear behavior of cellulose microfibers in wood-based hydrogels. Zhou et al. (Zhou et al., 2019) took into account the real fabrication process of the fiber-reinforced hydrogels and considered the nonlinear mechanical response of embedded fibers. However, in the abovementioned studies, only one or two families of fibers (a fiber family includes all the fibers aligned along one direction) are considered, which is suitable for anisotropic hydrogels with macro-sized fibers but inadequate to capture the microfiber-reinforced hydrogels often featuring complex microfiber distribution. Recently, Astruc et al. (Astruc et al., 2019) outlined an anisotropic constitutive model for soft fibrous tissue by taking into account both the distribution of microfibers and the nonlinear fiber behavior. Nevertheless, the interaction of water molecules with polymer/cellulose chains is not implemented into the model, such that the knowledge obtained from their study cannot be directly applied to understand the behavior of anisotropic hydrogels, in particular, the wood-based hydrogels.

In this study, we develop a physics-based constitutive model of microfiber-reinforced hydrogels (μFRG) by conceptualizing the material as a three-dimensional distribution of microfibers embedded in an isotropic hydrogel matrix. In particular, the model is suitable to simulate the mechanical response of wood-based hydrogels (i.e., hydrogels reinforced by micro-sized

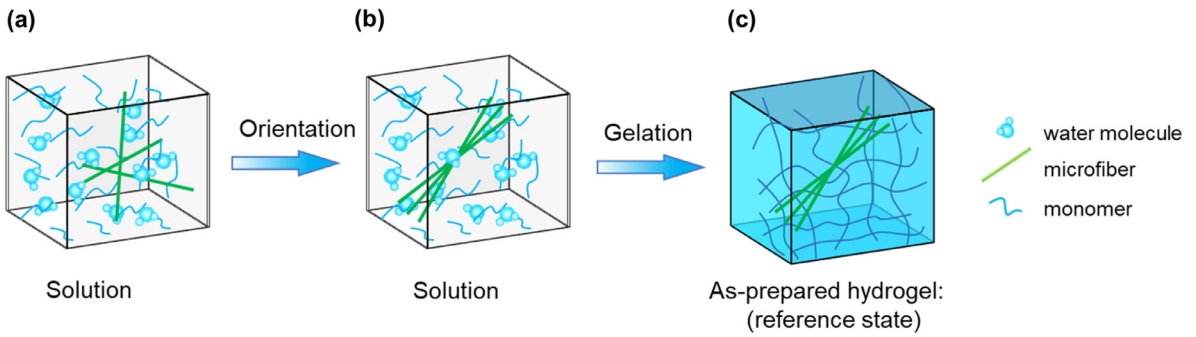

Fig. 1. A step-by-step representation of microfiber-reinforced hydrogel preparation processes. (a) A solution mixture of solvent, monomer molecules, and microfibers. (b) Orientation of the fibers. (c) As-prepared μFRG.

cellulose bundles), a novel anisotropic hydrogel system that has not been analyzed theoretically. Some of our theoretical results are compared to available experimental data of wood-based hydrogels in the literature. The unique nonlinear mechanical behavior of cellulose microfibers is discussed. The rest of this paper is organized as follows. In Section 2, we construct the constitutive models by resorting to a micromechanical treatment of the strain energy associated with the deformed microfibers. The restriction of a limited number of microfiber families is relaxed, and the microfibers can be described more precisely by a directional distribution. The equations of states, i.e., the stress-deformation relations are derived in the most generic form. In Section 3, the generic form of the μFRG constitutive model is fleshed out to model hydrogels with different types of fiber distribution. The anisotropic mechanical behaviors of these μFRG are investigated. In Section 4, the theory is further applied to study the actuation behaviors of a humidity-sensitive soft actuator where a thin layer of anisotropic wood-based hydrogel dries on a substrate. The bending actuation due to the dehydration of an anisotropic wood-based hydrogel film is compared with an in-plane isotropic wood-based hydrogel. Section 5 summarizes the main findings of the paper.

2. Constitutive model for microfiber reinforced anisotropic hydrogels

2.1. The fabrication and structure of microfiber-reinforced hydrogels

Fig. 1 describes a representative preparation process of a μFRG: As a first step, monomers and microfibers such as cellulose bundles are uniformly mixed in a solution or ink (Gladman et al., 2016; Markstedt et al., 2015; Siqueira et al., 2017; Torres-Rendon et al., 2015; Wang et al., 2016). Next, the external driving force is applied to orient the microfiber to the desired direction and extent of dispersion. For instance, both shear force due to solution/ink flow (Chen et al., 2014; Compton and Lewis, 2014) and externally applied electromagnetic field (Kokkinis et al., 2015; Lian et al., 2013) are reported as effective techniques to align microfibers in a controllable manner. Lastly, the gelation process is triggered to crosslink the monomers into a polymeric network. In the condition that the monomers are uniformly dissolved in the solvent and each monomer molecule is surrounded by abundant water molecules, it can be assumed that the presence of microfibers does not disturb or alter the gelation of the hydrogel phase. In other words, the existence of microfibers in the monomer aqueous solution does not intervene the gelation process chemically. In reverse, the gelation process itself is also independent of the microfibers mechanically. As a result, gelation and cross-linking do not induce any localized stress between the gel matrix and fibers. That is, the as-fabricated μFRG is stress-free. Such a free-swelling state is characterized by zero net stresses through the hydrogel since the stress due to network stretch and osmotic stress balance out (Hong et al., 2008).

2.2. Free energy function

This section specifies the free-energy density function which represents the intrinsic material properties of the μFRG. One notes that it is important to choose the correct normalization volume for the strain energy density of materials with changing volume. Herein, we take the as-prepared free-swelling state of the μFRG illustrated in Fig. 1c as the reference state. The free energy density W of the μFRG consists of the contribution from the isotropic hydrogel matrix and contribution from the deformed microfibers embedded in the matrix. That is, the total free energy density of the μFRG can be calculated by adding the free energy stored in the deformed microfibers W_{fiber} to that of the gel matrix W_{gel}, namely,

$$W = W_{\text{gel}} + W_{\text{fiber}} \tag{1}$$

A hydrogel is an aggregate of a network of crosslinked polymer chains and water molecules. Accordingly, from a thermodynamics perspective, W_{gel} can be postulated as a summation of the strain energy density W_{network} associated with the stretching of the polymer network and the entropic free energy density W_{mix} stemming from the mixing of the polymer

network and the water molecules, i.e., $W_{\text{gel}} = W_{\text{network}} + W_{\text{mix}}$. It has been widely recognized that the Helmholtz energy of the hydrogel divided by the volume of the dry polymer network is given by (Hong et al., 2009, 2010)

$$W'_{\text{gel}}(\mathbf{F}', \mu) = \frac{NkT}{2}\left(I'_1 - 3 - 2\log J'\right) - \frac{kT}{\nu}\left[\nu C \log\left(1 + \frac{1}{\nu C}\right) + \frac{\chi}{1+\nu C}\right] - \mu C \tag{2}$$

where N is the number of polymeric chains per unit volume of the dry polymer, C the nominal concentration of water defined as the number of water molecules in a unit volume of the dry polymer, $\nu = 3 \times 10^{-29}\text{m}^3$ is the volume per water molecule, χ the Flory-Huggins parameter measuring the hydrophilicity of the polymer network, and μ the chemical potential of water molecules, k is the Boltzmann constant, and T is the temperature in Kelvin scale. $I'_1 = F'_{iK}F'_{iK}$ and $J' = \det \mathbf{F}'$ are the first invariant and third invariant (Jacobian determinant). Note that the superscript ' is indicative of quantities defined on the dry state of the polymer network, such that $\mathbf{F}'$ is the deformation gradient tensor defined with respect to the dry polymer network. As discussed above, the free energy of the fiber-reinforced hydrogel consists of three terms: W_{network}, W_{mix}, and W_{fiber}. Notably, the energy of mixing W_{mix} is related to the number of permissible arrangements of gel monomers and solvent molecules in a lattice model. The introduction of fibers may change the number of possible arrangements and thus the energy of mixing. That is to say, the embedded fibers may affect the free energy of hydrogel through both W_{mix} and W_{fiber}. The object of this paper is to demonstrate how the complex microfiber distribution, which is taken into account by W_{fiber}, contributes to the anisotropic response of fiber-reinforced hydrogels. To focus on the main idea of this paper, for convenience, we assume the introduction of fibers does not affect the energy of mixing and adopt the best-known free-energy due to Flory and Rehner (Flory and Rehner, 1943) in Eq. (2).

We need to correlate the free energy density W'_{gel} given in Eq. (2) to the free energy density W_{gel} defined on the as-fabricated state of μFRG. The as-fabricated state of μFRG is dictated by the isotropic free swelling of the hydrogel phase. Consequently, relative to the dry polymer network, the as-prepared state of the μFRG sketched in Fig. 1c is characterized by the deformation gradient

$$\mathbf{F}_0 = \begin{bmatrix} \Lambda_0 & & \\ & \Lambda_0 & \\ & & \Lambda_0 \end{bmatrix} \tag{3}$$

with Λ_0 being the free-swelling stretch. One notes that Λ_0 relates to the chemical potential and the material properties $N\nu$ and χ by

$$N\nu\left(\Lambda_0^{-1} - \Lambda_0^{-3}\right) + \log\left(1 - \Lambda_0^{-3}\right) + \Lambda_0^{-3} + \chi\Lambda_0^{-6} - \mu_0/kT = 0 \tag{4}$$

where μ_0 is the chemical potential of water molecules when the μFRG is fabricated. Define $\mathbf{F}$ as the deformation gradient tensor of the current state relative to the as-fabricated state, namely, the reference state. The multiplicative decomposition of the deformation gradient gives that

$$\mathbf{F}' = \mathbf{F}\mathbf{F}_0 \tag{5}$$

Eq. (5) yields the relation between F'_{iK} and F_{iK} that

$$F'_{iK} = F_{iK}\Lambda_0 \tag{6}$$

Using the as-fabricated state of the μFRG as the reference state, we can express the free-energy density W_{gel} in terms of W'_{gel} as

$$W_{\text{gel}} = \Lambda_0^{-3} W'_{\text{gel}} \tag{7}$$

Substituting Eqs. (6) and (7) into Eq. (2) gives the free energy density defined in the reference state (namely, free energy divided by the volume of as-fabricated μFRG)

$$W_{\text{gel}}(\mathbf{F}, \mu) = \frac{NkT}{2\Lambda_0^3}\left[F_{iK}F_{iK}\Lambda_0^2 - 3 - 2\log\left(J\Lambda_0^3\right)\right] - \frac{kT}{\nu\Lambda_0^3}\left[\nu C \log\left(1 + \frac{1}{\nu C}\right) + \frac{\chi}{1+\nu C} + \frac{\mu}{kT}\nu C\right] \tag{8}$$

Since the embedded fibers do not imbibe solvent and thus does not change volume, it is postulated that the volume change of the fiber-reinforced hydrogels is fully transmitted to the hydrogel phase consisting of polymer network and water. By further assuming both parties are incompressible, we obtain a relation between the nominal water concentration C and the volume of μFRG that

$$J' = J\Lambda_0^3 = 1 + \nu C \tag{9}$$

where $J = \det(\mathbf{F})$ is the volume ratio relative to the reference state. Subject to the constraint (9), the water concentration C is not independent but is expressed in terms of the deformation gradient $\mathbf{F}$. A combination of Eq. (8) and Eq. (9) gives

$$W_{\text{gel}}(\mathbf{F}, \mu) = \frac{NkT}{2\Lambda_0^3}\left[I_1\Lambda_0^2 - 3 - 2\log\left(J\Lambda_0^3\right)\right] - \frac{kT}{\nu\Lambda_0^3}\left[\left(J\Lambda_0^3 - 1\right)\log\left(\frac{J\Lambda_0^3}{J\Lambda_0^3 - 1}\right) + \frac{\chi}{J\Lambda_0^3} + \frac{\mu}{kT}\left(J\Lambda_0^3 - 1\right)\right] \tag{10}$$

where $I_1 = F_{iK}F_{iK}$.

The microfibers embedded in the μFRG feature a homogeneous and anisotropic distribution, which is described by a probability distribution function of the fiber orientation angles $\rho(\theta, \phi)$, where $\theta \in [0, 2\pi)$ represents the circumferential angle and $\phi \in [0, \pi]$ is the meridional angle. The distribution function $\rho(\theta, \phi)$ satisfies that $\int_0^{2\pi}\int_0^{\pi}\rho(\theta,\phi)\sin\phi d\phi d\theta = 1$. The orientation of each microfiber is characterized by a unit direction vector $\boldsymbol{N}(\theta,\phi) = \cos\theta\sin\phi\boldsymbol{e_1} + \sin\theta\sin\phi\boldsymbol{e_2} + \cos\phi\boldsymbol{e_3}$. To study the deformation of microfibers, we hypothesize that the microfiber-microfiber contact is negligible. In the language of mechanics of composite materials, the fiber reinforcement phase is "diluted". Along this line, the microfibers are assumed to deform affinely with the macroscopic deformation gradient $\mathbf{F}$, such that the macroscopic stretch of a microfiber can be calculated by

$$\lambda^{\mathrm{f}}(\theta,\phi) = \sqrt{\boldsymbol{N}\cdot\boldsymbol{C}\boldsymbol{N}} \tag{11}$$

where $\mathbf{C} = \mathbf{F}^{\mathrm{T}}\mathbf{F}$ is the right Cauchy-Green deformation tensor. Hence the energy stored in one strained microfiber can be expressed in terms of the macroscopic deformation $\mathbf{F}$ and the fiber orientation $\boldsymbol{N}(\theta,\phi)$, that is, $U_{\mathrm{fiber}} = U_{\mathrm{fiber}}(\mathbf{F}|\boldsymbol{N})$. The strain energy density of microfibers can be determined by integrating the strain energy density of all fibers over all orientations weighted by the probability density distribution $\rho(\theta, \phi)$ as

$$W_{\mathrm{fiber}}(\mathbf{F}) = \int_0^{2\pi}\int_0^{\pi} U_{\mathrm{fiber}}(\boldsymbol{F}|\boldsymbol{N})\rho(\theta,\phi)\sin\phi d\phi d\theta \tag{12}$$

Eq. (12) can also be written as an integral extends over a unit sphere that $W_{\mathrm{fiber}} = \iint U_{\mathrm{fiber}}(\mathbf{F}|\boldsymbol{N})\rho(\theta,\phi)dA$, where $dA = \sin\phi d\phi d\theta$ is the infinitesimal area element.

By assembling Eqs. (10) and (12) into Eq. (1), we arrive at an expression for the total strain energy density of the μFRG

$$\begin{aligned} W(\mathbf{F},\mu) = {} & \frac{NkT}{2\Lambda_0^3}\left[I_1\Lambda_0^2 - 3 - 2\log\left(J\Lambda_0^3\right)\right] \\ & - \frac{kT}{\nu\Lambda_0^3}\left[\left(J\Lambda_0^3 - 1\right)\log\left(\frac{J\Lambda_0^3}{J\Lambda_0^3 - 1}\right) + \frac{\chi}{J\Lambda_0^3} + \frac{\mu}{kT}\left(J\Lambda_0^3 - 1\right)\right] \\ & + \int_0^{2\pi}\int_0^{\pi} U_{\mathrm{fiber}}(\mathbf{F}|\boldsymbol{N})\rho(\theta,\phi)\sin\phi d\phi d\theta \end{aligned} \tag{13}$$

After defining the free energy function W, the nominal stress can be derived as

$$S_{iK} = \frac{\partial W(\mathbf{F},\mu)}{\partial F_{iK}} \tag{14}$$

In particular, principal nominal stress in the μFRG is given by

$$\begin{aligned} \frac{S_i}{kT/v} = {} & \frac{N\nu}{\Lambda_0^2}\left(\Lambda_0\lambda_i - \frac{1}{\Lambda_0\lambda_i}\right) + \frac{1}{\Lambda_0^3\lambda_i}\left[J\Lambda_0^3\log\left(1 - \frac{1}{\Lambda_0^3 J}\right) + 1 + \frac{\chi}{\Lambda_0^3 J} - \frac{\mu}{kT}J\Lambda_0^3\right] \\ & + \frac{\nu}{kT}\int_0^{2\pi}\int_0^{\pi}\frac{\partial U_{\mathrm{fiber}}}{\partial\lambda^{\mathrm{f}}}\frac{\partial\lambda^{\mathrm{f}}}{\partial\lambda_i}\rho(\theta,\phi)\sin\phi d\phi d\theta \end{aligned} \tag{15}$$

where S_i (i=1, 2, 3) is the principal stress and λ_i the corresponding principal stretch. The first two terms in Eq. (15) are the stresses stemming from the deformation of the macroscopic hydrogel and the last term is contributed by the length change of the embedded microfibers. Note that the macroscopic stretch of a microfiber can be expressed in terms of the principal stretch λ_i as $\lambda^{\mathrm{f}}(\theta,\phi) = \sqrt{(\lambda_1\sin\phi\cos\theta)^2 + (\lambda_2\sin\phi\sin\theta)^2 + (\lambda_3\cos\phi)^2}$, so that the derivative of the macro-stretch is given by

$$\frac{\partial\lambda^{\mathrm{f}}}{\partial\lambda_1} = \frac{\lambda_1\sin^2\phi\cos^2\theta}{\lambda^{\mathrm{f}}} \tag{16–1}$$

$$\frac{\partial\lambda^{\mathrm{f}}}{\partial\lambda_2} = \frac{\lambda_2\sin^2\phi\sin^2\theta}{\lambda^{\mathrm{f}}} \tag{16–2}$$

$$\frac{\partial\lambda^{\mathrm{f}}}{\partial\lambda_3} = \frac{\lambda_3\cos^2\phi}{\lambda^{\mathrm{f}}} \tag{16–3}$$

2.3. The mechanical behavior of microfibers

The constitutive model derived in the previous section leaves the strain energy function U_{fiber} unspecified. We now discuss a particular way to represent the mechanical behavior of microfibers. In the macroscale, a common treatment for fiber elasticity is to adopt a linear elastic model that features a linear stiffness in both tension and compression. However, given

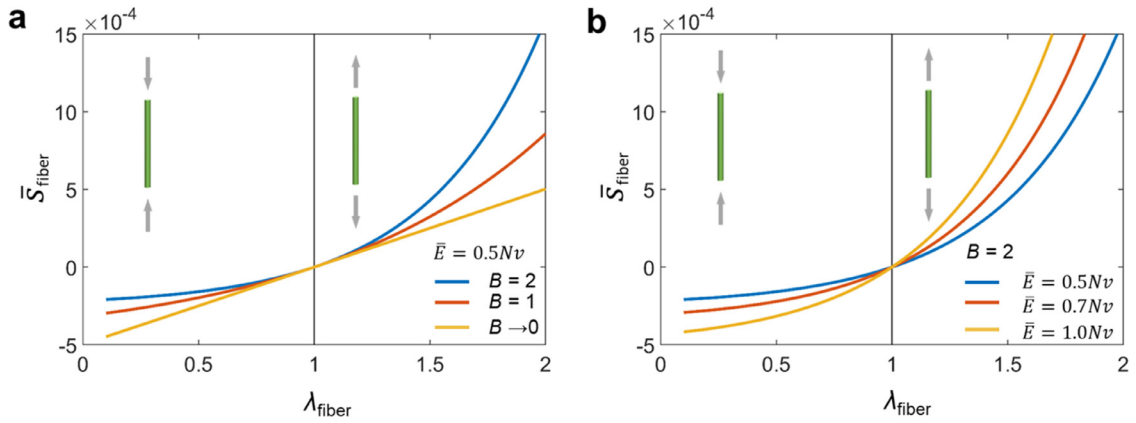

Fig. 2. Elastic properties of a single microfiber. (a) The dependence of the fiber stress-stretch relation on parameter B. (b) The dependence of the fiber stress-stretch relation on parameter $\bar{E}$.

its large aspect ratio, the microfibers of concern are more deformable to compression than to stretching, rendering the mechanical behavior of microfibers highly nonlinear. Hereby, we assume an exponential Fung-type stress response (Fung, 1967) for a single microfiber, which was originally intended for soft tissue fibrils such as collagen fibers, that

$$S_{\text{fiber}} = \frac{\partial U_{\text{fiber}}}{\partial \lambda^{\text{f}}} = \frac{E}{B}\left[e^{B(\lambda^{\text{f}}-1)} - 1\right] \tag{17}$$

where E and B are two model parameters: E is the fiber stiffness at infinitesimal strain, and B is a dimensionless shape parameter with positive values. Note that for convenience E incorporates the fiber volume fraction. It is worth noting that the Fung-type model was developed to capture the response of collagen fibers in tension, but not in compression, because collagen fibers are crimped in the initial configuration (Lu et al., 2018) and they cannot support compression. The main focus of this paper will be on anisotropic wood-based hydrogels reinforced by cellulose fibers. In contrast to the crimped collagen fibers, cellulose fibers embedded in hydrogels can sustain some degrees of compression for three reasons: (1) Cellulose fibers are straight and uncrimped, such that they can sustain compression before buckling. (2) Cellulose fibers embedded in hydrogels are surrounded by hydrogel matrix and neighboring cellulose fibers, the lateral deflection of the fibers, which is necessary for the onset of fiber buckling, is thus constrained. Therefore, cellulose fibers in hydrogels are not as susceptible to buckling as freestanding cellulose fibers. (3) Even if buckling sets in, further lateral deflection required by the post-buckling deformation is strongly restricted by the surrounding matrix and fibers, such that the post-buckled fibers can still sustain modest compression. In summary, the cellulose fibers embedded in hydrogels can support some degrees of compression, contrasting with the crimped collagen fibers. In addition, experimental evidence has accumulated that cellulose fibers under tension also feature a nonlinear behavior (Kong et al., 2018). Moreover, it should be noted that the framework of the current theory is not restricted to the use of the Fung-type model given by Eq. (17). It can readily adopt other models. For example, to model hydrogels reinforced by collagen fibers of zero compressive strength, a modified Fung-type model developed by following a 'tension-compression switch' approach (Holzapfel and Ogden, 2015) can be employed. Details of the modified Fung-type model is given in Appendix A.

To describe the contribution of microfibers to the stress of μFRG, we can introduce a normalized stiffness for microfibers $\bar{E} = Ev/kT$ and the associated normalized fiber stress $\bar{S}_{\text{fiber}} = S_{\text{fiber}}v/kT$. The dependence of the microfiber stress-strain relation on parameter B is shown in Fig. 2a. When B approaches zero, the mechanical behavior of the microfiber is rather linearly elastic. When B takes a finite positive value, the stress response becomes nonlinear: the magnitude of tensile stiffness is larger than the stiffness in compression. The nonlinearity of the stress response increases as B increases, so that the higher the value of B, the stiffer the microfiber. The effect of $\bar{E}$ is straightforward, as shown in Fig. 2b, the fiber stiffness increases with increasing $\bar{E}$.

2.4. The equations of state of microfiber-reinforced hydrogels

A combination of Eqs. (15-17) gives the generic expression of the nominal principal stresses of μFRGs with arbitrary microfiber distributions,

$$\begin{aligned}\frac{S_1}{kT/v} = {} & \frac{Nv}{\Lambda_0^2}\left(\Lambda_0\lambda_1 - \frac{1}{\Lambda_0\lambda_1}\right) + \frac{1}{\Lambda_0^3\lambda_1}\left[J\Lambda_0^3\log\left(1-\frac{1}{\Lambda_0^3 J}\right) + 1 + \frac{\chi}{\Lambda_0^3 J} - \frac{\mu}{kT}J\Lambda_0^3\right] \\ & + \int_0^{2\pi}\int_0^{\pi}\frac{\bar{E}}{B}\left[e^{B(\lambda^{\text{f}}-1)} - 1\right]\frac{\lambda_1\sin^2\phi\cos^2\theta}{\lambda^{\text{f}}}\rho(\theta,\phi)\sin\phi d\phi d\theta\end{aligned} \tag{18–1}$$

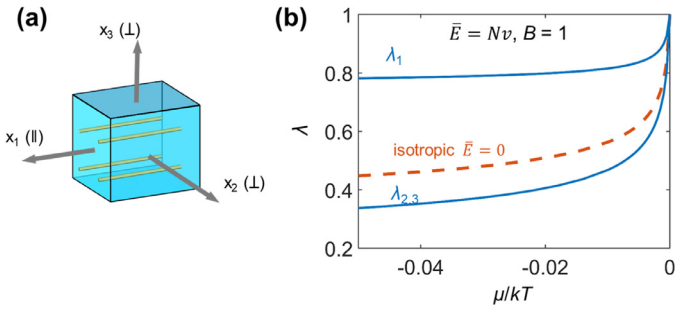

Fig. 3. Anisotropic free-dehydration of μFRG with microfibers perfectly aligned in one direction. (a) Schematic of the μFRG. All microfibers are perfectly aligned in x_1 direction. (b) The anisotropic deformation of the μFRG due to free dehydration with $\bar{E} = N\nu$ and $B = 1$. The dehydration of an isotropic hydrogel without embedded microfibers is plotted as the baseline case.

$$\frac{S_2}{kT/v} = \frac{N\nu}{\Lambda_0^2}\left(\Lambda_0\lambda_2 - \frac{1}{\Lambda_0\lambda_2}\right) + \frac{1}{\Lambda_0^3\lambda_2}\left[J\Lambda_0^3\log\left(1 - \frac{1}{\Lambda_0^3 J}\right) + 1 + \frac{\chi}{\Lambda_0^3 J} - \frac{\mu}{kT}J\Lambda_0^3\right] + \int_0^{2\pi}\int_0^{\pi}\frac{\bar{E}}{B}\left[e^{B(\lambda^{\mathrm{f}}-1)} - 1\right]\frac{\lambda_2\sin^2\phi\sin^2\theta}{\lambda^{\mathrm{f}}}\rho(\theta,\phi)\sin\phi d\phi d\theta \tag{18–2}$$

$$\frac{S_3}{kT/v} = \frac{N\nu}{\Lambda_0^2}\left(\Lambda_0\lambda_3 - \frac{1}{\Lambda_0\lambda_3}\right) + \frac{1}{\Lambda_0^3\lambda_3}\left[J\Lambda_0^3\log\left(1 - \frac{1}{\Lambda_0^3 J}\right) + 1 + \frac{\chi}{\Lambda_0^3 J} - \frac{\mu}{kT}J\Lambda_0^3\right] + \int_0^{2\pi}\int_0^{\pi}\frac{\bar{E}}{B}\left[e^{B(\lambda^{\mathrm{f}}-1)} - 1\right]\frac{\lambda_3\cos^2\phi}{\lambda^{\mathrm{f}}}\rho(\theta,\phi)\sin\phi d\phi d\theta \tag{18–3}$$

Eqs. (18) are the equations of state relating the stress of the μFRG to the deformation gradient $\mathbf{F}$ when a μFRG is held at a constant chemical potential. Given the chemical potential μ, the parameter χ describing the enthalpy of mixing, and the microfiber distribution function $\rho(\theta, \phi)$, the three stretches λ_1, λ_2, and λ_3 can be determined once the applied stresses σ_1, σ_2, and σ_3 are known, and vice versa. The equations of state have three adjustable materials parameters: $N\nu$ is a dimensionless measure of the hydrogel stiffness, $\bar{E}$ is the normalized fiber stiffness and B is a parameter dictating the nonlinearity of the stress response of microfibers. In all the application cases to come in the following sections, if not otherwise mentioned, we will take the values being: $\mu_0 = 0$, $\chi = 0.2$, $N\nu = 10^{-3}$. It is worth noting that the as-fabricated hydrogels are usually not fully swollen, such that the initial chemical potential μ_0 is less than zero and its exact value needs to be calibrated by experiments. The focus of this work is on developing the theoretical framework and applying it to the anisotropic hydrogels reinforced by cellulose fibers. Without loss of generality, we set $\mu_0 = 0$ for simplification. Assigning a negative value to μ_0 will not change the major conclusions of this work.

3. Anisotropic mechanical behaviors of microfiber-reinforced hydrogels

This section examines the anisotropic behaviors of μFRGs with three distinct types of fiber distributions: (1) perfectly aligned microfibers, (2) microfibers uniformly distributed in a plane, and (3) microfibers following in-plane von Mises distribution.

3.1. Anisotropic hydrogel with perfectly aligned microfibers

The configuration of the μFRG with perfectly aligned microfibers is depicted schematically in Fig. 3(a). Such an idealized case is suitable when most of the microfibers are highly aligned (Kong et al., 2018; Mredha et al., 2018). Without losing generality, the microfibers are assumed to be arranged in parallel along the x_1 direction, such that the probability distribution function $\rho(\theta, \phi)$ reduces to the Dirac delta function. In the language of composite materials, the μFRG with perfectly aligned microfibers is transversely isotropic with the x_2x_3-plane being the plane of isotropy. The equations of state shown in Eqs. (18) take the form

$$\frac{S_1}{kT/v} = \frac{N\nu}{\Lambda_0^2}\left(\Lambda_0\lambda_1 - \Lambda_0^{-1}\lambda_1^{-1}\right) + \Lambda_0^{-3}\lambda_1^{-1}\left[J\Lambda_0^3\log\left(1 - \frac{1}{J\Lambda_0^3}\right) + 1 + \frac{\chi}{J\Lambda_0^3} - \frac{\mu}{kT}J\Lambda_0^3\right] + \frac{\bar{E}}{B}\left[e^{B(\lambda_1-1)} - 1\right] \tag{19–1}$$

$$\frac{S_2}{kT/v} = \frac{N\nu}{\Lambda_0^2}\left(\Lambda_0\lambda_2 - \Lambda_0^{-1}\lambda_2^{-1}\right) + \Lambda_0^{-3}\lambda_2^{-1}\left[J\Lambda_0^3\log\left(1 - \frac{1}{J\Lambda_0^3}\right) + 1 + \frac{\chi}{J\Lambda_0^3} - \frac{\mu}{kT}J\Lambda_0^3\right] \tag{19–2}$$

$$\frac{S_3}{kT/v} = \frac{N\nu}{\Lambda_0^2}\left(\Lambda_0\lambda_3 - \Lambda_0^{-1}\lambda_3^{-1}\right) + \Lambda_0^{-3}\lambda_3^{-1}\left[J\Lambda_0^3\log\left(1 - \frac{1}{J\Lambda_0^3}\right) + 1 + \frac{\chi}{J\Lambda_0^3} - \frac{\mu}{kT}J\Lambda_0^3\right] \tag{19–3}$$

We first study the free swelling/dehydration behavior of such a μFRG from its as-synthesized state. This process can be modeled by setting stresses given in Eqs. (19) to be zero, namely,

$$S_i = 0 \tag{20}$$

where i=1, 2, and 3. The state of deformation of μFRGs can be characterized by the longitudinal stretch λ_1 and two transverse stretches $\lambda_2 = \lambda_3$, so that Eq. (20) have two independent equations, $S_1 = 0$ and $S_2 = S_3 = 0$, which are used to determine the two independent stretches. Fig. 3b plots the free-dehydration stretch as a function of the chemical potential. With the chemical potential of the solvent μ/kT decreasing from μ_0/kT =0 to −0.05, the μFRG shrinks continuously. As a baseline case, we plot the dehydration curve of an isotropic hydrogel without any embedded microfibers by setting the microfiber stiffness $\bar{E} = 0$ (orange line in Fig. 3b). As expected, the hydrogel dehydrates with isotropic stretches: $\lambda_1 = \lambda_2 = \lambda_3$. In contrast, in the presence of microfibers (namely, $\bar{E} > 0$), the μFRG shrinks in an anisotropic manner with $\lambda_1 \neq \lambda_2 = \lambda_3$. In Fig. 3b, we take μFRG with $\bar{E} = N\nu$ and $B = 1$ as an example. Due to the existence of the microfibers, the deformation of μFRG in the x_1 direction is strongly constrained, therefore the contraction along the fiber direction is less than that in the two transverse directions. Consequently, the anisotropic dehydration behavior of μFRG is characterized by two distinct curves: the λ_1 curve is located above the baseline case and $\lambda_{2,3}$ curve falls below the baseline case.

We next study the anisotropic mechanical behavior of the μFRG under uniaxial tension. The anisotropy in mechanical properties of the μFRG implicates that stretching the μFRG along different directions may yield different resulting stresses. To demonstrate this, we examine two cases: The μFRG is subject to uniaxial tension along the microfiber direction x_1 (Case 1, Fig. 4a) or the transverse direction x_2 (Case 2, Fig. 4b). For Case 1, the state of deformation is characterized by the longitudinal stretch λ_1 and the transverse stretch $\lambda_2 = \lambda_3$. The stresses in the transverse direction equal zero, so that

$$\frac{N\nu}{\Lambda_0^2}\left(\Lambda_0\lambda_2 - \Lambda_0^{-1}\lambda_2^{-1}\right) + \Lambda_0^{-3}\lambda_2^{-1}\left[\lambda_1\lambda_2^2\Lambda_0^3\log\left(1 - \frac{1}{\lambda_1\lambda_2^2\Lambda_0^3}\right) + 1 + \frac{\chi}{\lambda_1\lambda_2^2\Lambda_0^3} - \frac{\mu}{kT}\lambda_1\lambda_2^2\Lambda_0^3\right] = 0 \tag{21}$$

Given a longitudinal stretch λ_1, Eq. (21) determines the transverse stretch $\lambda_2 = \lambda_3$. The magnitude of the stress S_1 is given by Eq. (19–1). For Case 2, the uniaxial tension along the x_2 direction induces anisotropic contraction in the x_1x_3-plane, with $\lambda_1 \neq \lambda_3$. The stresses in the x_1 and x_3 directions vanish, thus

$$\frac{N\nu}{\Lambda_0^2}\left(\Lambda_0\lambda_1 - \Lambda_0^{-1}\lambda_1^{-1}\right) + \Lambda_0^{-3}\lambda_1^{-1}\left[\lambda_1\lambda_2\lambda_3\Lambda_0^3\log\left(1 - \frac{1}{\lambda_1\lambda_2\lambda_3\Lambda_0^3}\right) + 1 + \frac{\chi}{\lambda_1\lambda_2\lambda_3\Lambda_0^3} - \frac{\mu}{kT}\lambda_1\lambda_2\lambda_3\Lambda_0^3\right] + \frac{\bar{E}}{B}\left[e^{B(\lambda_1-1)} - 1\right] = 0 \tag{22–1}$$

$$\frac{N\nu}{\Lambda_0^2}\left(\Lambda_0\lambda_3 - \Lambda_0^{-1}\lambda_3^{-1}\right) + \Lambda_0^{-3}\lambda_3^{-1}\left[\lambda_1\lambda_2\lambda_3\Lambda_0^3\log\left(1 - \frac{1}{\lambda_1\lambda_2\lambda_3\Lambda_0^3}\right) + 1 + \frac{\chi}{\lambda_1\lambda_2\lambda_3\Lambda_0^3} - \frac{\mu}{kT}\lambda_1\lambda_2\lambda_3\Lambda_0^3\right] = 0 \tag{22–2}$$

Eqs. (22) determine the stretch λ_1 and λ_3 given an applied stretch λ_2. Then Eq. (19–2) relates the stress S_2 to the stretch λ_2. We plot the resulting stress as a function of the applied stretch for both cases in Fig. 4c-4f, with different values of $\bar{E}$ or B. As expected, stretching the μFRG along the microfiber direction (i.e., Case 1, blue line in Fig. 4c-4f) results in much higher stress than stretching in the transverse direction (i.e., Case 2, orange line), which is attributed to the reinforcement effect due to microfibers. Moreover, one notes that the microfiber stiffness decreases from Fig. 4c to 4f, since the fiber stiffness reduces with decreasing $\bar{E}$ or B as analyzed above. Fig. 4c-4f show that the difference between the two cases becomes more pronounced for μFRG with stiffer microfibers (i.e., with higher $\bar{E}$ and B). However, no apparent difference is observed between the transverse stress-stretch relations in all these four cases. This can be attributed to the fact that there is no intrinsic inter-fiber interaction in the transverse direction and in such direction the material property is dominated by the hydrogel phase.

Another aspect of the anisotropic mechanical behavior of the μFRG is reflected by the anisotropic contraction in the cross-section normal to the applied stretching. In particular, when the μFRG is subjected to tension in x_2 direction (Fig. 5a), the contraction of the x_1x_3-plane is anisotropic, which features two independent stretches λ_1 and λ_3. Therefore, the shape of the cross-section during stretching is represented by the trajectory of the curves shown in Fig. 5b. As λ_2 increases from 1 to 6 (indicated by the arrow direction in Fig. 5b), a family of these trajectories is parametrized by the stiffness of microfibers $\bar{E}$. The baseline case of isotropic hydrogel without microfibers ($\bar{E}$=0) exhibits an equal contraction since the λ_3-λ_1 curve extends along the 45° line on which $\lambda_1 = \lambda_3$. For μFRG with positive $\bar{E}$, the λ_3-λ_1 curve deviates from the isotropic baseline case: the contraction in the microfiber direction (x_1) is less obvious compared to the contraction in the transverse direction (x_3), so that the λ_3-λ_1 curve of μFRG always lies below the baseline case. We plot in Fig. 5c that the volumetric ratio J as a function of the applied stretch λ_2. The monotonically increasing J indicates that the μFRG continues to take in water as it gets elongated. The results in Fig. 5c intriguingly suggest that μFRG with stiffer microfibers tends to be more capable of water uptake. The effect of distribution of microfibers on the water absorption will be further discussed below.

To validate the theoretical model, in Fig. 6, we compare the theoretical prediction to the experimentally measured stress-strain curves of wood-based hydrogels reported in the literature (Kong et al., 2018). The samples were polyacrylamide (PAM) hydrogels reinforced by stiff cellulose fibers highly aligned along the longitudinal direction of the gel and the hydrogels were stretched along the fiber direction (i.e., the Case 1 discussed above). One notes that the tensile tests were performed

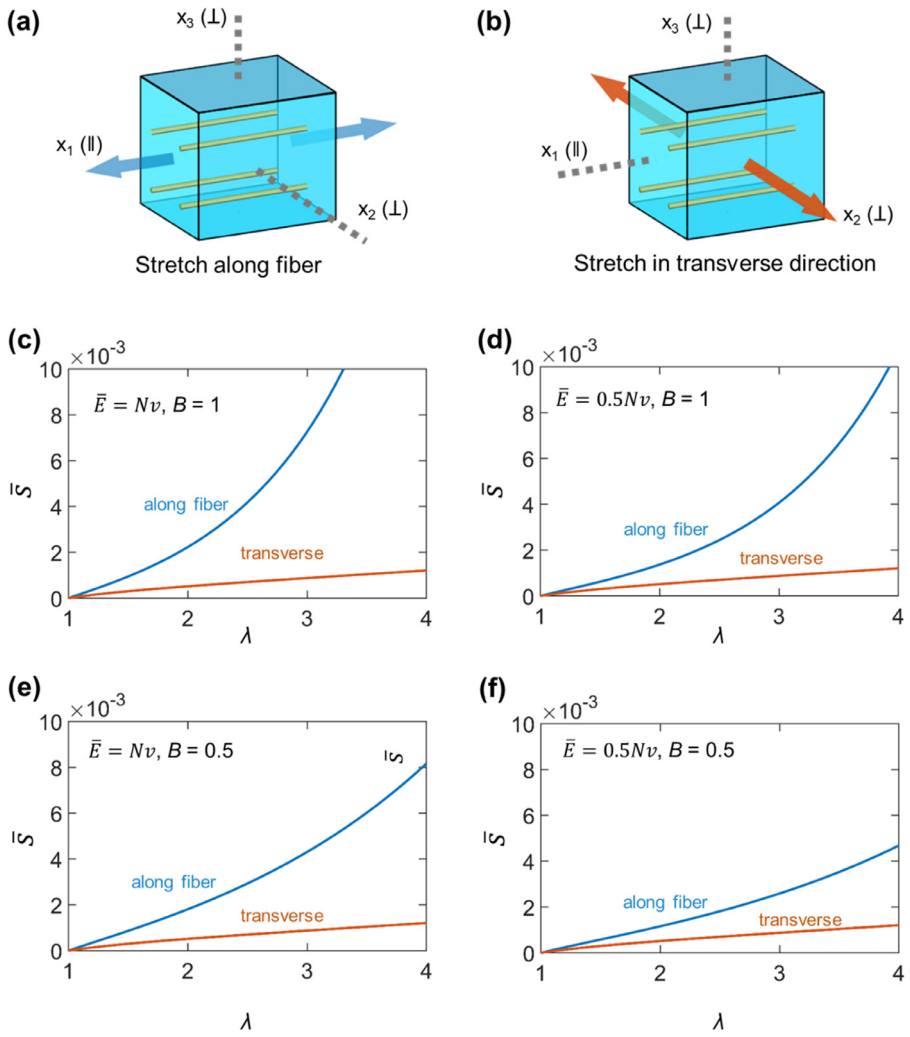

Fig. 4. Anisotropic stress response of μFRG with microfibers perfectly aligned in x_1 direction. Schematics of the μFRG under uniaxial tension (a) along the microfiber direction and (b) in the transverse direction. Stress due to stretching the μFRG along the microfiber direction (blue lines) and stretching along the transverse direction (orange lines) are plotted with various fiber properties: (c) $\bar{E} = N\nu$, $B = 1$, (d) $\bar{E} = 0.5N\nu$, $B = 1$, (e) $\bar{E} = N\nu$, $B = 0.5$, and (f) $\bar{E} = 0.5N\nu$, $B = 0.5$.

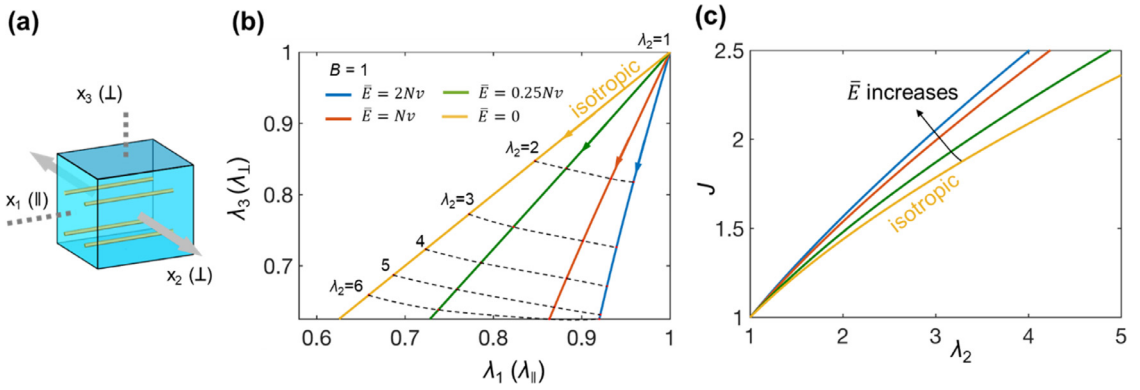

Fig. 5. Anisotropic contraction of the μFRG. (a) Schematic of a μFRG under uniaxial tension along the x_2 direction. (b) The anisotropic stretches along the x_1 direction (namely, the fiber direction) and the x_3 direction are shown for various microfiber stiffness: $\bar{E} = 2N\nu$, $\bar{E} = N\nu$, $\bar{E} = 0.25N\nu$, and $\bar{E} = 0$ (isotropic hydrogel without embedded microfibers). (c) Effect of the fiber stiffness on the water uptake.

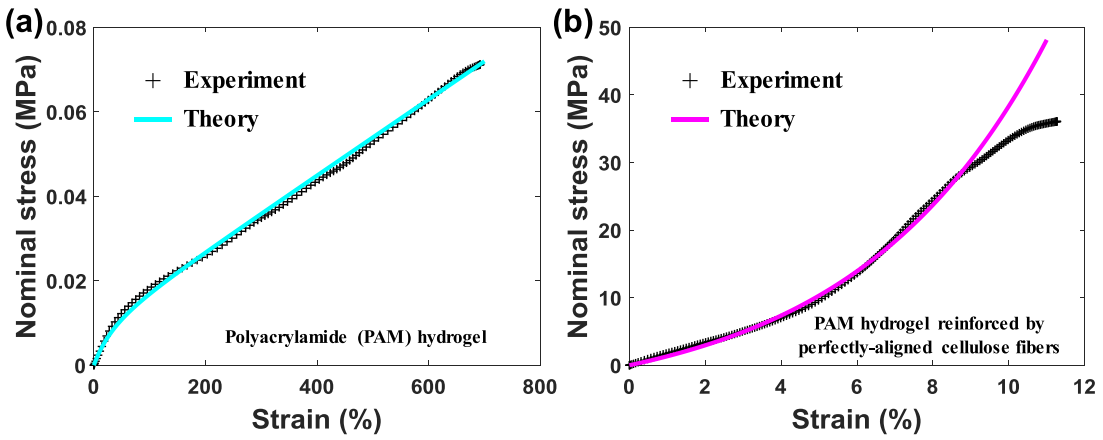

Fig. 6. The comparison of the experimentally measured and theoretically predicted stress-strain behaviors of the polyacrylamide (PAM) hydrogels reinforced by cellulose fibers. (a) A pure PAM hydrogel is tested to determine the stiffness of the PAM hydrogel phase. (b) One sample of cellulose-fiber-reinforced PAM hydrogels is tested under uniaxial tension. The following parameters are adopted to make the plot: $NkT/\Lambda_0 = 9$ kPa, $B = 20$, $E = 120$ MPa. The experimental data are taken from the literature (Kong et al., 2018).

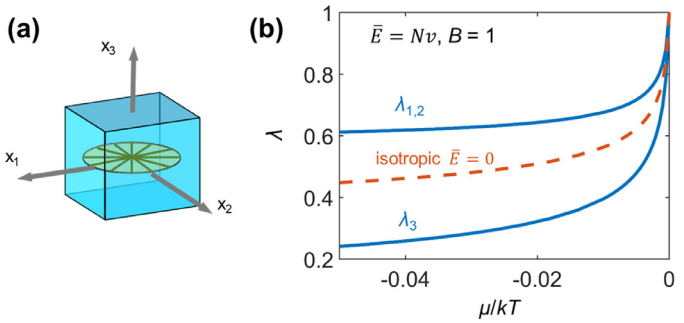

Fig. 7. Anisotropic deswelling behavior of μFRG with microfibers featuring an in-plane uniform distribution. (a) Schematic of the μFRG. (b) Anisotropic stretches due to free dehydration of the μFRG. Here $\bar{E} = N\nu$ and $B = 1$.

in the air, not in contact with water, such that the wood-based hydrogels could not imbibe water, resulting in a constant volume during testing with a fixed volumetric ratio J. The corresponding stress-strain relationship can be developed based on Eq. (13). The details of the formulation are given in Appendix B. Fig. 6a shows the data that are used to determine the stiffness of the pure PAM hydrogel, giving $NkT/\Lambda_0 = 9$ kPa. In Fig. 6b, the theoretical predictions of the stress-strain behavior of cellulose-fibers-reinforced PAM hydrogels match the experimental results consistently by setting $B = 20$, $E = 120$ MPa. It is noted that the experimentally observed stiffening behavior of the wood-based hydrogels is well captured by the theoretical results (Fig. 6b). The experimentally measured stress-strain curve deviates from the theoretical prediction at the high strain level. The discrepancy may stem from the damage of the cellulose fibers that we have not taken into account in the current model.

3.2. Anisotropic hydrogel with microfibers featuring an in-plane uniform distribution

The μFRG with uniformly distributed microfibers in a plane is depicted schematically in Fig. 7a. For example, such an arrangement can be made possible when the thickness dimension of the hydrogel is much smaller than the in-plane dimensions (Kuang et al., 2019). Without loss of generality, the microfibers are assumed to be arranged uniformly in the x_1x_2-plane, so that the in-plane probability density function takes the form

$$\rho(\theta) = 1/2\pi \tag{23}$$

where θ is the circumferential angle defined in the x_1x_2-plane. The μFRG with microfibers featuring an in-plane uniform distribution is transversely isotropic, with the x_1x_2-plane in which microfibers are distributed being the plane of isotropy. The equations of state take the form

$$\frac{S_1}{\kappa T/\nu} = \frac{N\nu}{\Lambda_0^2}\left(\Lambda_0\lambda_1 - \Lambda_0^{-1}\lambda_1^{-1}\right) + \Lambda_0^{-3}\lambda_1^{-1}\left[J\Lambda_0^3\log\left(1 - \frac{1}{J\Lambda_0^3}\right) + 1 + \frac{\chi}{J\Lambda_0^3} - \frac{\mu}{kT}J\Lambda_0^3\right]$$
$$+\frac{\bar{E}}{2\pi B}\int_0^{2\pi}\left[e^{B\left(\lambda^f-1\right)} - 1\right]\frac{\lambda_1\cos^2\theta}{\lambda^f}d\theta \tag{24–1}$$

$$\frac{S_2}{\kappa T/\nu}=\frac{N\nu}{\Lambda_0^2}\left(\Lambda_0\lambda_2-\Lambda_0^{-1}\lambda_2^{-1}\right)+\Lambda_0^{-3}\lambda_2^{-1}\left[J\Lambda_0^3\log\left(1-\frac{1}{J\Lambda_0^3}\right)+1+\frac{\chi}{J\Lambda_0^3}-\frac{\mu}{kT}J\Lambda_0^3\right]$$
$$+\frac{\bar{E}}{2\pi B}\int_0^{2\pi}\left[e^{B\left(\lambda^f-1\right)}-1\right]\frac{\lambda_2\sin^2\theta}{\lambda^f}d\theta \tag{24–2}$$

$$\frac{S_3}{\kappa T/\nu}=\frac{N\nu}{\Lambda_0^2}\left(\Lambda_0\lambda_3-\Lambda_0^{-1}\lambda_3^{-1}\right)+\Lambda_0^{-3}\lambda_3^{-1}\left[J\Lambda_0^3\log\left(1-\frac{1}{J\Lambda_0^3}\right)+1+\frac{\chi}{J\Lambda_0^3}-\frac{\mu}{kT}J\Lambda_0^3\right] \tag{24–3}$$

Given an applied loading such as free-dehydration and uniaxial tension, equations of state can be obtained by setting the appropriate stress components in Eqs. (24) to be zero.

The free dehydration of such a μFRG can be modeled by taking $S_i=0$ (i =1, 2, 3). The anisotropic dehydration features two independent stretches $\lambda_1=\lambda_2$ and λ_3. Fig. 7b plots the stretches as a function of the chemical potential. In making the plot, we take $\bar{E}=N\nu$, $B=1$. The microfibers are arranged in x_1x_2-plane in a uniform manner, thereby reinforcing the in-plane stiffness of the μFRG. Consequently, the μFRG undergoes less contraction in the x_1x_2-plane than that in the direction perpendicular to the plane. The baseline case with $\bar{E}=0$ is plotted as the orange dashed line in Fig. 7b, demonstrating the isotropic deswelling behavior of isotropic hydrogel. Should $\bar{E}$ diminish from $N\nu$ to 0, both the in-plane and out-of-plane stretch curves of μFRG will merge to the baseline-case curve.

We next exemplify the anisotropic behavior of μFRGs by studying the stress responses due to uniaxial tension along the in-plane direction (Fig. 8a) and out-of-plane direction (Fig. 8b). In Fig. 8c-8f, we plot the in-plane and out-of-plane uniaxial stress-stretch relations for four combinations of the mechanical properties of microfibers. Owning to the reinforcement effect of microfibers, the in-plane stress is higher than the out-of-plane stress by several folds. From Fig. 8c to 8f, the difference between the in-plane stress response and the out-of-plane stress response becomes less profound, because of the reduction in fiber stiffness. A comparison between Fig. 4 and Fig. 8 shows that the μFRGs with microfibers uniformly distributed in a plane are more deformable than the μFRGs with perfectly aligned fibers.

We also examine the anisotropic contraction of μFRG in response to uniaxial tension along the in-plane direction (x_2), as illustrated in Fig. 9a. The λ_3-λ_1 curves in Fig. 9b show the shape evolution of x_1x_3 cross-section as λ_2 increases from 1 to 5 (arrow direction). The baseline case of isotropic hydrogel without microfibers ($\bar{E}$ =0) still extends along the 45° line. Intriguingly, even though the in-plane stiffness is reinforced by the distributed microfibers, the μFRG is rather more deformable in the in-plane direction (x_1) than in the out-of-plane direction (x_3), as shown in Fig. 9b. Therefore, all λ_3-λ_1 curves in Fig. 9b are located above the baseline curve, in stark contrast to the results shown in Fig. 5b. This counterintuitive finding can be understood as follows. When a piece of hydrogel is uniaxially elongated, there exist two competing mechanisms underpinning its deformation: The uniaxial stretch along x_2 direction causes the x_1x_3 cross-section to contract due to the Poisson's effect, while the contraction is compensated by the expansion of hydrogel due to water absorption. The existence of microfibers intervenes the competition of these two mechanisms through its spatial distribution. As in the case discussed in Section 3.1 (Fig. 5a), the resistance to contraction in the x_1 direction contributed by the perfectly aligned microfibers is considerable, so that the material contracts much more readily in the out-of-plane x_3 direction. Therefore, the deformation of the μFRG is dictated by the mechanism of Poisson's effect. In contrast, when the microfibers are uniformly distributed in the x_1x_2-plane (Fig. 9a), the resistance against the contraction in the x_1 direction significantly diminishes and thus the magnitude of contraction due to Poisson's effect along the x_1 and x_3 directions are comparable. For this reason, the expansion due to water absorption becomes the dominating factor in determining the final shape of the x_1x_3 cross-section: the hydrogel expands more in the x_3 direction, rendering the overall out-of-plane contraction less than that in the x_1 direction. More intriguingly, the out-of-plane dimension of the cross-section does not deform monotonically as the μFRG gets stretched in the x_1 direction. For example, the magnitude of λ_3 corresponding to $\bar{E}=0.25N\nu$ reduces at first but then increases, which further indicates that the expansion due to water absorption in the x_3 direction becomes increasingly dominant as the hydrogel elongates along the x_2 direction. We plot the volume ratio J as a function of the applied stretch λ_2 in Fig. 9c. It can be concluded that the water absorption is bounded and the μFRG containing stiffer microfibers tends to absorb less water, which is in contrast to the μFRG with perfectly aligned microfibers, suggesting that the water absorption behavior of μFRG can be programmed by tuning the microfiber distribution.

3.3. Anisotropic hydrogel with microfibers following in-plane von Mises distribution

In general, the microfibers are not necessarily perfectly aligned or follow a uniform in-plane arrangement in μFRG. For instance, the fiber alignment extent is usually affected by the applied stimuli during fabrication (Mredha et al., 2018; Omidinia-Anarkoli et al., 2017; Tseng et al., 2014). As a more general case, we next examine the μFRGs with microfibers following an in-plane von Mises distribution (Tonge et al., 2013; Xiao et al., 2016). The probability distribution function of the von Mises distribution is given by

$$\rho(\theta|\theta_0,\ \kappa)=\frac{e^{\kappa\cos 2(\theta-\theta_0)}}{2\pi I_0(\kappa)} \tag{25}$$

where θ_0 indicates the dominant fiber direction in the plane where microfibers lie in, angle θ denotes the fiber orientation angle in the plane and $\theta-\theta_0$ ranges from 0 to π, κ is the concentration factor measuring the spread of the fiber distribution

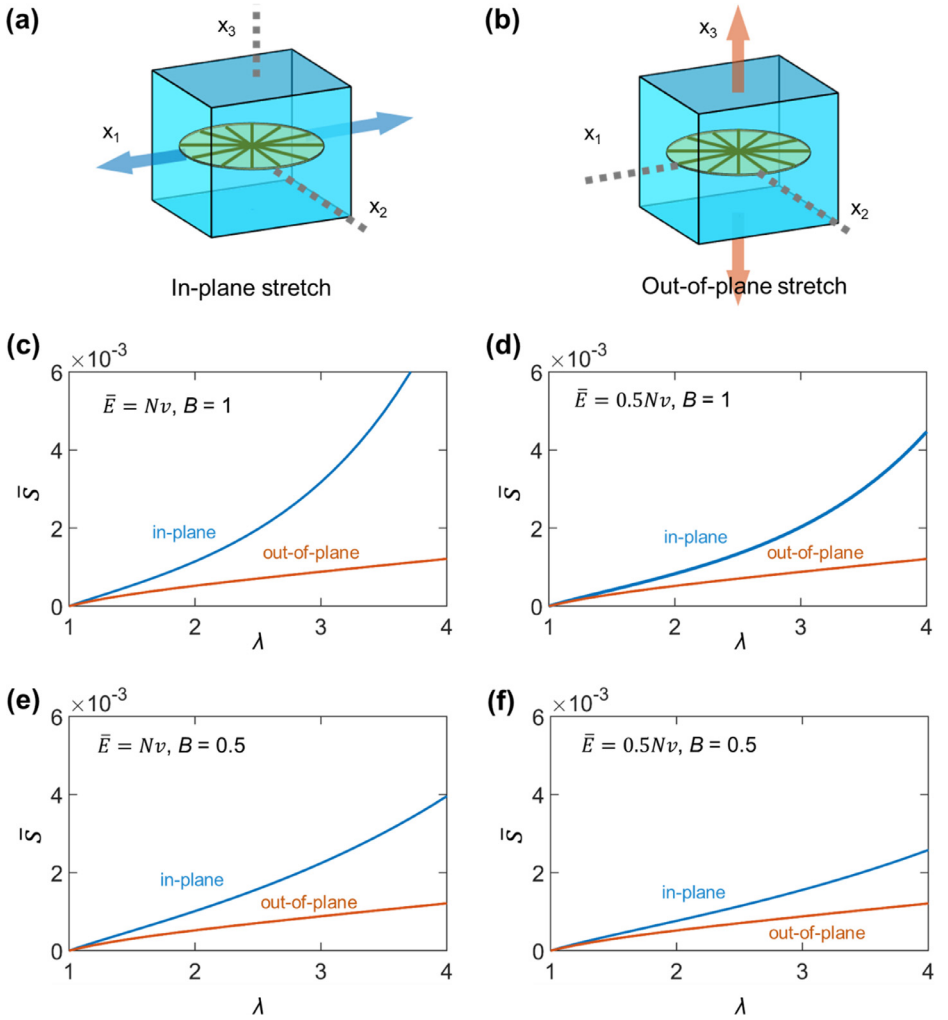

Fig. 8. Anisotropic stress response of μFRGs with microfibers following an in-plane uniform distribution. Schematics of μFRGs subjected to uniaxial tension (a) in the x_1x_2-plane and (b) in the direction normal to the plane. Stress-stretch relation of μFRGs with different microfiber properties are presented: (c) $\bar{E} = N\nu$, $B = 1$, (d) $\bar{E} = 0.5N\nu$, $B = 1$, (e) $\bar{E} = N\nu$, $B = 0.5$, and (f) $\bar{E} = 0.5N\nu$, $B = 0.5$.

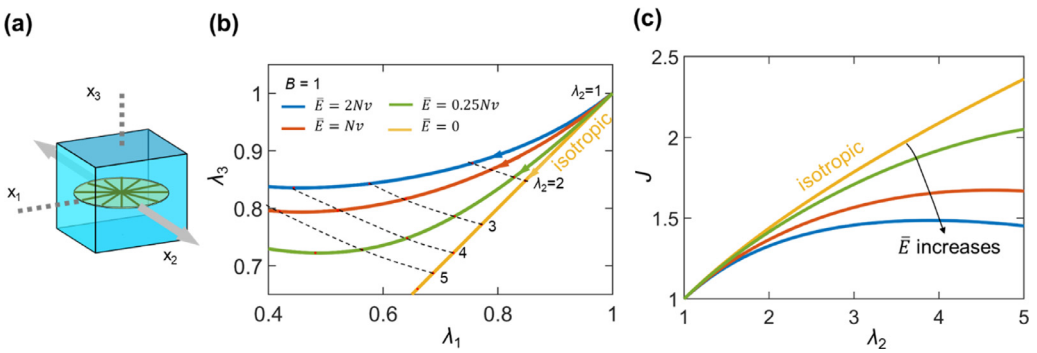

Fig. 9. Anisotropic contraction of the cross-section perpendicular to the loading direction. (a) Schematic of uniaxial loading in the x_2 direction. (b) Contraction of the x_1x_3 cross-section for four cases: $\bar{E} = 2N\nu$, $\bar{E} = N\nu$, $\bar{E} = 0.25N\nu$, and $\bar{E} = 0$ (isotropic hydrogel without microfibers). (c) Volume ratio as a function of applied stretch λ_2.

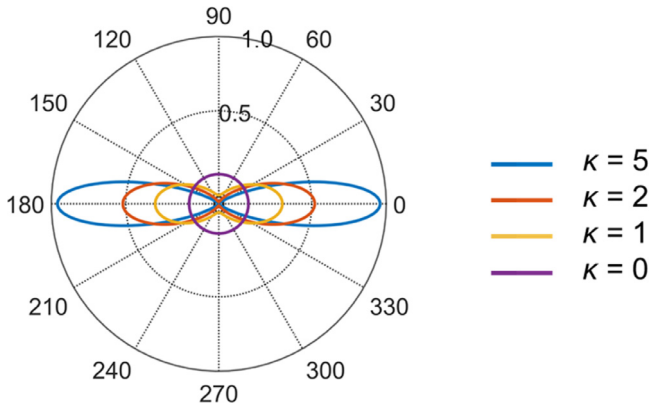

Fig. 10. Polar plot of the von Mises distribution of microfibers with concentration parameter κ =5, 2, 1, and 0 (uniform in-plane distribution). The fiber mean direction θ_0 is taken to be 0 in making the plot.

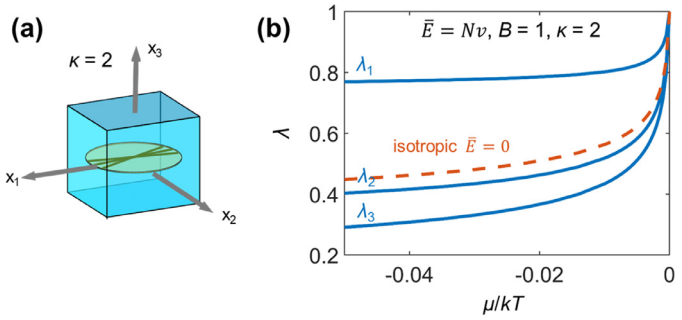

Fig. 11. Free dehydration of μFRG with microfibers following in-plane von Mises distribution (a) Schematic of the μFRG. (b) Anisotropic free deswelling of the μFRG. Here, $\bar{E} = N\nu$, $B = 1$, and κ=2.

around the preferred orientation θ_0, and $I_0(\kappa) = \frac{1}{\pi}\int_0^{\pi} e^{\kappa\cos\theta}d\theta$ is the first-kind hyperbolic Bessel function of order zero. Plotted in Fig. 10 is the microfiber distribution at different concentration factors. The microfibers are highly concentrated if κ is large; and become perfectly aligned as discussed in Section 3.1 when $\kappa \to \infty$. If κ is zero, the microfiber distribution recovers the in-plane uniform distribution discussed in Section 3.2.

The μFRG with microfibers characterized by von Mises distribution with κ =2 is depicted schematically in Fig. 11a. The microfibers are assumed to be arranged in the x_1x_2-plane and the x_1 direction is taken to be the dominant fiber direction (then θ_0 is set to be 0 for simplicity). Unlike the transversely-isotropic μFRGs analyzed in Section 3.1 and Section 3.2, the μFRG with microfibers following in-plane von Mises distribution is orthotropic. Equations of state are given in terms as the principal stresses and stretches,

$$\frac{S_1}{kT/v} = \frac{N\nu}{\Lambda_0^2}\left(\Lambda_0\lambda_1 - \Lambda_0^{-1}\lambda_1^{-1}\right) + \Lambda_0^{-3}\lambda_1^{-1}\left[J\Lambda_0^3\log\left(1-\frac{1}{J\Lambda_0^3}\right) + 1 + \frac{\chi}{J\Lambda_0^3} - \frac{\mu}{kT}J\Lambda_0^3\right] + \frac{\bar{E}}{2\pi I_0(\kappa)B}\int_0^{2\pi}\left[e^{B\left(\lambda^{\mathrm{f}}-1\right)}-1\right]\frac{e^{\kappa\cos 2\theta}\lambda_1\cos^2\theta}{\lambda^{\mathrm{f}}}d\theta \tag{26-1}$$

$$\frac{S_2}{kT/v} = \frac{N\nu}{\Lambda_0^2}\left(\Lambda_0\lambda_2 - \Lambda_0^{-1}\lambda_2^{-1}\right) + \Lambda_0^{-3}\lambda_2^{-1}\left[J\Lambda_0^3\log\left(1-\frac{1}{J\Lambda_0^3}\right) + 1 + \frac{\chi}{J\Lambda_0^3} - \frac{\mu}{kT}J\Lambda_0^3\right] + \frac{\bar{E}}{2\pi I_0(\kappa)B}\int_0^{2\pi}\left[e^{B\left(\lambda^{\mathrm{f}}-1\right)}-1\right]\frac{e^{\kappa\cos 2\theta}\lambda_2\sin^2\theta}{\lambda^{\mathrm{f}}}d\theta \tag{26-2}$$

$$\frac{S_3}{kT/v} = \frac{N\nu}{\Lambda_0^2}\left(\Lambda_0\lambda_3 - \Lambda_0^{-1}\lambda_3^{-1}\right) + \Lambda_0^{-3}\lambda_3^{-1}\left[J\Lambda_0^3\log\left(1-\frac{1}{J\Lambda_0^3}\right) + 1 + \frac{\chi}{J\Lambda_0^3} - \frac{\mu}{kT}J\Lambda_0^3\right] \tag{26-3}$$

The μFRG studied here is orthotropic so that the free dehydration of the μFRG is characterized by three independent stretches $\lambda_1 \neq \lambda_2 \neq \lambda_3$, which are shown as three curves in Fig. 11b. When subjected to chemical potential change, the μFRG undergoes the largest contraction along the x_3 direction because of the lack of microfibers and the smallest shrinkage

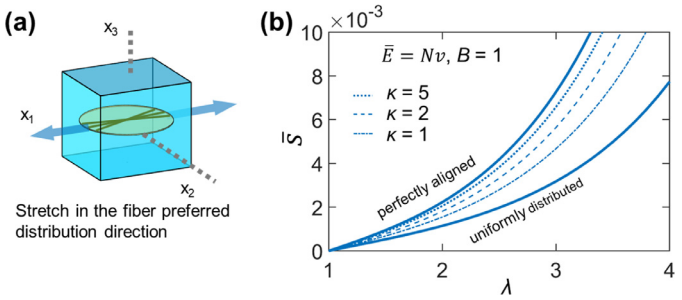

Fig. 12. Stress response of μFRG under uniaxial tension. (a) Schematic of μFRG with microfibers featuring in-plane von Mises distribution. The μFRG is stretched along the fiber-rich direction. (b) The stress-stretch relation with different values of κ. All curves are sandwiched by two limiting cases, namely, the case with perfectly-aligned microfibers ($\kappa = \infty$) and the case with uniformly-distributed microfibers ($\kappa = 0$).

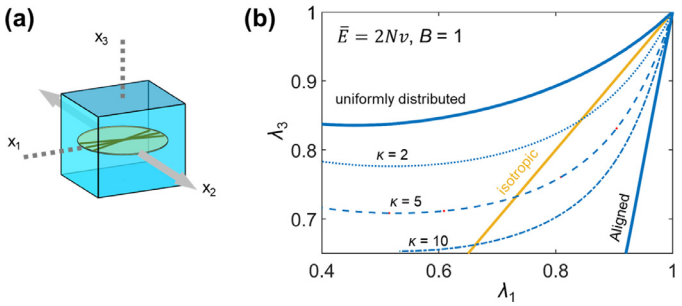

Fig. 13. Anisotropic contraction of the cross-section perpendicular to the uniaxial tension. (a) Schematic of a μFRG with microfibers featuring von Mises distribution subjected to uniaxial tension along x_2 direction. (b) The two stretches characterizing the shape change of the x_1x_3 cross-section. All curves are sandwiched by the two limiting cases.

along the x_1 direction due to strong reinforcement. The dehydration of hydrogel without any microfibers are illustrated as the baseline case.

A μFRG under uniaxial stretch along the dominant fiber direction, namely, the x_1 direction, is schematically sketched in Fig. 12a. The stress response as a function of the applied stretch is plotted in Fig. 12b, with various values of κ. As expected, the stress-stretch curves with κ =1, 2, 5 are bounded by the two limiting cases: the case of perfectly-aligned microfibers ($\kappa = \infty$) which sets the upper bound and the case of in-plane uniformly-distributed microfibers ($\kappa = 0$) which delineates the lower bound. The stiffness of the μFRG along the stretching direction strongly depends on the spread of the fiber orientation: The more concentrated the fiber distribution (i.e., the larger κ), the stiffer the μFRG.

We also examine the μFRG subjected to uniaxial stretch along the in-plane fiber-poor direction, namely, the x_2 direction, as illustrated in Fig. 13a. The shape shifting of the x_1x_3 cross-section is described by the two stretches λ_1 and λ_3. The relation between the two stretches is shown in Fig. 13b with different values of κ. All λ_3-λ_1 curves are sandwiched by the two limiting cases of $\kappa = \infty$ and $\kappa = 0$. As κ decreases, the λ_3-λ_1 curve shifts from the bottom right of the figure to the upper left corner. The shifting can be attributed to the competition between the two deformation mechanisms mentioned in the preceding discussion on Fig. 9b: If the microfiber distribution is highly concentrated (i.e., κ is large), the μFRG is significantly stiffened along the microfiber-rich direction so that the contraction in this direction (x_1) due to Poisson's effect is less than that in the out-of-plane direction (x_3). However, as the microfiber distribution gets more dispersed, the deformation of μFRG becomes dominated by the expansion due to water absorption. The contraction along x_3 induced by Poisson's effect is largely offset by the water-imbibing-induced expansion, such that the μFRG undergoes larger contraction along the x_1 direction.

In this section, we have explored the basic aspects of μFRGs featuring various microfiber orientations, including the anisotropic free dehydration and anisotropic mechanical response under uniaxial tension. We will next apply the constitutive model to wood-based hydrogels and investigate the deformation of a wood-hydrogel-based soft actuator.

4. Modeling soft actuators driven by the drying of a wood-based hydrogel

4.1. Wood-based hydrogels and soft actuator based on wood-based hydrogels

Among the widespread applications of anisotropic soft materials, soft actuators capitalizing the anisotropic deformation to achieve optimized actuation performance have garnered tremendous attentions. Recently, Kuang et al. developed a bi-layer soft actuator by exploiting the drying of a wood-based hydrogel film with selectively aligned cellulose microfibers

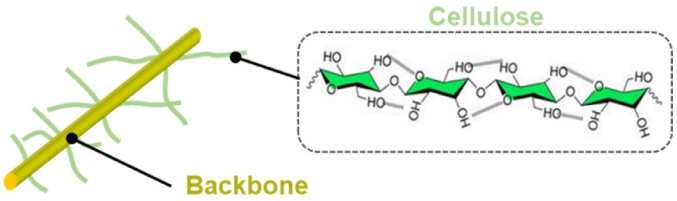

Fig. 14. Structure of chemically treated cellulose fibers. Cellulose microfibers (bundled CNFs) act as backbone providing strength and stiffness. The exposed cellulose nanofibers tethered to the backbone bundle are hydrophilic and can attract water molecules via hydrogen bonds.

(Kuang et al., 2019). To construct the wood-based hydrogel, micro-sized natural cellulose fibers are processed through a chemo-mechanical treatment which is widely adopted in the paper-making industry. The structure of a post-treatment cellulose fiber is featured by a cellulose microfiber serving as the backbone with hydrophilic cellulose nanofibers tethered to the backbone surface, as schematically illustrated in Fig. 14. The microfiber backbone is formed by the bundling of CNFs during the treatment. The nano-sized CNFs attached to the backbone possess a large number of hydroxyl groups that facilitate the formation of inter-molecular bonding between individual CNFs and thereby assemble into a percolated CNF network. Once brought into contact with water, the CNF network takes in water, eventually developing into a wood-based hydrogel. It is worth noting that the wood-based hydrogel, by nature, is a microfiber reinforced hydrogel (μFRG): As sketched in Fig. 14, the micro-sized backbone bundle acts as the reinforcement phase which provides stiffness and mechanical strength; CNFs tethered to the backbone form a hydrophilic network, absorbing and retaining water molecules. To this end, the swelling/dehydration and deformation of the wood-based hydrogel can be simulated by the constitutive model formulated in Section 2, by approximating the mechanical behavior of CNFs by Gaussian chain model.

Kuang et al. constructed a wood-hydrogel-based soft actuator by attaching a wood-based hydrogel (WG) film to a passive polyimide (PI) substrate, as illustrated in Fig. 15a and 15b. Since the wood-based hydrogel is prepared in an aqueous solution with relative humidity (RH) of 100%, exposing the bilayer actuator to air environment of $RH<100\%$ (recall the chemical potential of water is related to RH through $\mu = kT\log RH$) may expel water from the wood-based hydrogel. The resultant water loss is accompanied by a significant decrease in the volume of WG, while the volume of the PI substrate remains unchanged, thereby driving the actuation of the bilayer to scroll up toward the WG side. The orientation of the cellulose microfibers, i.e., the backbone, can be tuned by the evaporation-assisted circulation flow, such that the WG/PI actuator can be fabricated with microfibers aligned parallel to the width of the WG film (see schematic of the structure in the top panel of Fig. 15a). Compared to the WG/PI actuator with randomly-distributed cellulose microfibers (bottom panel of Fig. 15a), it has been experimentally revealed that a WG/PI actuator with aligned microfibers exhibits an enhanced actuation performance, as schematically shown in Fig. 15b.

4.2. Analysis and results

The bilayer bending problem driven by differential deformation is a classic topic of mechanics of materials. An analytical solution was provided by Timoshenko to the bending of linear elastic bilayers due to the mismatch in thermal expansion between the two layers (Timoshenko, 1925). Unfortunately, this specific problem of wood-based hydrogel drying on a polyimide substrate is not one of the perfectly suitable cases for the Timoshenko's solution. The volumetric strain of wood-based hydrogel due to the loss of water is anisotropic and nonlinear, because of the arrangement of cellulose microfibers and the interaction between cellulose nanofibers and water molecules. Although it was a common practice to model the moisture absorption process of wood using a thermal expansion analogy, the nonlinear and anisotropic volumetric strains of the wood-based hydrogel due to water loss cannot be prescribed in an *a priori* manner but should be solved as part of the boundary value problem. The constitutive model for the μFRGs described in Section 2 directly links the anisotropic behavior of μFRGs to their microstructures, such that it is more physically rigorous to adopt the model to study the deformation mechanism of WG/PI soft actuator than to exploit the thermal-expansion analogy. As discussed in Section 2 and Section 3, the drying process of wood-based hydrogel can be modeled by varying the chemical potential μ. The volumetric strains of the wood-based hydrogel, namely, λ_1, λ_2, and λ_3, can be evaluated by solving the equations of state shown in Eq. (18) with appropriate boundary conditions.

Most general cases of bilayer bending do not lend themselves to analytical solutions where the bilayer structures are made of hyperelastic materials with finite thick plies, unless certain forms of the material constitutive are satisfied (Cabello et al., 2016; Kanner and Horgan, 2008; Tsai et al., 2004) or certain assumptions about the bending kinematics are made (Xiao, 2016). In demonstrating the present constitutive model for μFRGs, we focus our attention on the situation where the thickness of the wood-based hydrogel film is very thin compared to the thickness of the PI substrate. As a result, the material state variables (strain, stress, and water concentration, etc.) remain the same through the film thickness, so that the resultant force on the WG cross-section is given by

$$P = S_2 b h_{\mathrm{f}} \tag{27}$$

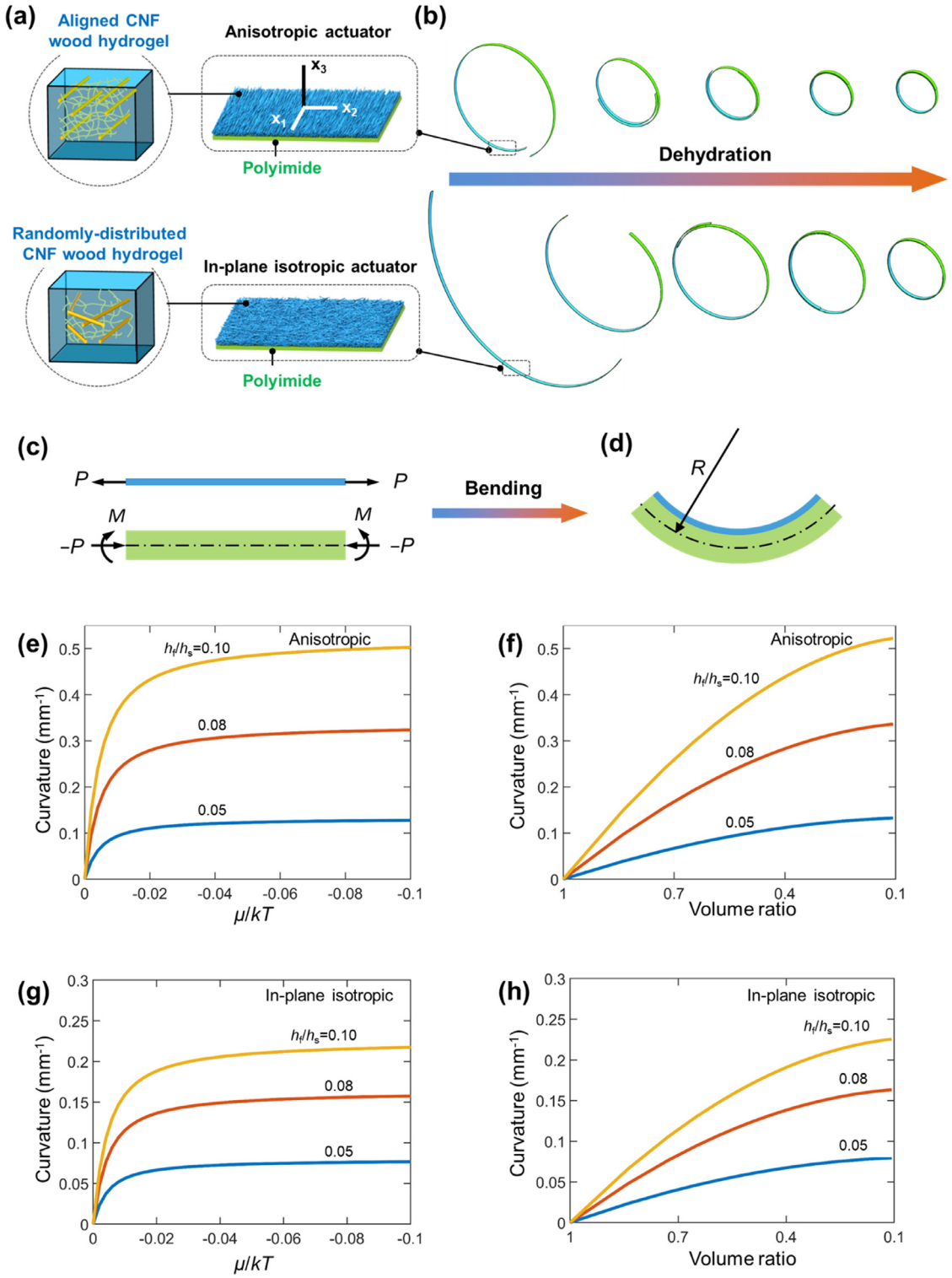

Fig. 15. Wood-based hydrogel (WG) film drying on a polyimide (PI) substrate. (a) Schematic of an anisotropic soft actuator with cellulose microfibers perfectly aligned along the width of the film and an isotropic actuator with microfibers randomly (i.e., uniformly) distributed in the wood-based hydrogel film. (b) An illustration of the sequential bending of the WG/PI soft actuator at various water loss levels. (Reproduced from (Kuang et al., 2019)) (c) Free body diagram of the bilayer upon WG film shrinkage. (d) Schematic of the bending of the bilayer. (e) Bending curvature of the anisotropic soft actuator as a function of chemical potential. (f) Bending curvature of the anisotropic soft actuator as a function of the volume ratio. (g) Bending curvature of the isotropic soft actuator as a function of chemical potential. (h) Bending curvature of the isotropic soft actuator as a function of the volume ratio.

where h_f and b are the thickness and the width of the wood-based hydrogel film, respectively. The resultant axial force P of the WG film is transferred to the PI substrate via the WG/PI interface, generating a moment M to the PI substrate and causing the bending of the entire bilayer structure (Fig. 15c). The bending moment is given by

$$M = Ph_s/2 \tag{28}$$

where h_s denotes the thickness of the PI substrate. Considering the slender PI substrate as an Euler beam, the bending radius R of the actuator can be obtained as

$$\frac{1}{R} = \frac{6P}{E_s h_s^2 b} \tag{29}$$

where E_s is Young's modulus of the substrate. The deformation compatibility requires that length of the WG film equals the length of the PI substrate at the interface, providing an additional equation relating the resultant force P to the longitudinal stretch λ_2 of the film as

$$\lambda_2 = -\frac{3P}{E_s h_s b} + 1 \tag{30}$$

Combining Eqs. (27) and (30), one gets that

$$S_2 = \frac{1-\lambda_2}{\frac{3}{E_s}\frac{h_f}{h_s}} \tag{31}$$

By taking the WG layer as a sufficiently thin film, the out-of-plane stress component (stress normal to the wood-based hydrogel surface) of the WG film vanishes, i.e., $S_3 = 0$. Moreover, contraction of the WG film along the width direction of the film is strongly restricted by the underlying PI substrate, such that $\lambda_1 = 1$. Therefore, for a WG/PI soft actuator with cellulose microfibers aligned parallel to the width of the film, the governing equations for the bending of the soft actuator is comprised of two independent equations that

$$\frac{N\nu}{\Lambda_0^2}\left(\Lambda_0\lambda_2 - \Lambda_0^{-1}\lambda_2^{-1}\right) + \Lambda_0^{-3}\lambda_2^{-1}\left[J\Lambda_0^3\log\left(1-\frac{1}{J\Lambda_0^3}\right) + 1 + \frac{\chi}{J\Lambda_0^3} - \frac{\mu}{kT}J\Lambda_0^3\right] = \frac{E_s\nu}{kT}\frac{1-\lambda_2}{3\frac{h_f}{h_s}} \tag{32-1}$$

$$\frac{N\nu}{\Lambda_0^2}\left(\Lambda_0\lambda_3 - \Lambda_0^{-1}\lambda_3^{-1}\right) + \Lambda_0^{-3}\lambda_3^{-1}\left[J\Lambda_0^3\log\left(1-\frac{1}{J\Lambda_0^3}\right) + 1 + \frac{\chi}{J\Lambda_0^3} - \frac{\mu}{kT}J\Lambda_0^3\right] = 0 \tag{32-2}$$

where $J = \lambda_2\lambda_3$. Eqs. (32) introduce two dimensionless parameters, $\frac{E_s\nu}{kT}$ being Young's modulus of the elastic PI substrate normalized by $\frac{kT}{\nu}$, and $\frac{h_f}{h_s}$ being the thickness ratio between the WG film and the PI substrate. In the following calculations, the material properties being used are, for hydrogel matrix $N\nu = 0.008$, $\chi = 0.2$; for microfibers the stiffness parameter $E = 2N\nu$, and the shape parameter $B = 1$; for the PI substrate, Young's modulus is estimated as $E_s = 5N\nu$.

Likewise, for the WG/PI soft actuator featuring randomly (uniformly)-distributed cellulose microfibers, the equations of state are

$$\frac{N\nu}{\Lambda_0^2}\left(\Lambda_0\lambda_2 - \Lambda_0^{-1}\lambda_2^{-1}\right) + \Lambda_0^{-3}\lambda_2^{-1}\left[J\Lambda_0^3\log\left(1-\frac{1}{J\Lambda_0^3}\right) + 1 + \frac{\chi}{J\Lambda_0^3} - \frac{\mu}{kT}J\Lambda_0^3\right] + \frac{\bar{E}}{2\pi B}\int_0^{2\pi}\left[e^{B(\lambda^f-1)} - 1\right]\frac{\lambda_2\sin^2\theta}{\lambda^f}d\theta = \frac{E_s\nu}{kT}\frac{1-\lambda_2}{3\frac{h_f}{h_s}} \tag{33-1}$$

$$\frac{N\nu}{\Lambda_0^2}\left(\Lambda_0\lambda_3 - \Lambda_0^{-1}\lambda_3^{-1}\right) + \Lambda_0^{-3}\lambda_3^{-1}\left[J\Lambda_0^3\log\left(1-\frac{1}{J\Lambda_0^3}\right) + 1 + \frac{\chi}{J\Lambda_0^3} - \frac{\mu}{kT}J\Lambda_0^3\right] = 0 \tag{33-2}$$

We solve Eqs. (32) and (33) for λ_2 and λ_3 at various chemical potential μ. Then the bending curvature is evaluated by plugging Eqs. (27) and (31) into Eq. (29). The volume ratio is obtained by using $J = \lambda_2\lambda_3$ ($\lambda_1 = 1$) as a measurement of the water loss level. The bending curvature (i.e., $1/R$), a measurement of the actuation performance, is plotted as a function of the chemical potential (Fig. 15e and 15g) and the volume ratio (Fig. 15f and 15h). As the chemical potential μ decreases, the WG film continues to lose water, giving rise to the increase of bending curvature. The degree of bending gradually saturates as water content is depleted (Fig. 15e and 15g). A comparison between the WG/PI actuator exhibiting aligned microfibers (Fig. 15e and 15f) with the actuator featuring uniformly-distributed microfibers (Fig. 15g and 15h) demonstrates that the anisotropic WG configuration enables a bending curvature 2 to 2.5 times higher than its isotropic counterpart. The superb performance of the anisotropic soft actuator can be understood as follows: When the cellulose microfibers are aligned along the width of the film, the contraction in the longitudinal direction of the active WG film is not intervened by the cellulose microfibers. In contrast, when the cellulose microfibers are randomly (i.e., uniformly) oriented, the contraction of the actuator is restricted by the cellulose microfibers, causing reduced bending curvature. In addition, all cases in Fig. 15 are solved at various thickness ratios of h_f/h_s. As expected, a thicker WG film leads to a larger actuation displacement. As the chemical potential decreases, the CNF hydrogel continues to lose water but the deformation approaches to a final shape as

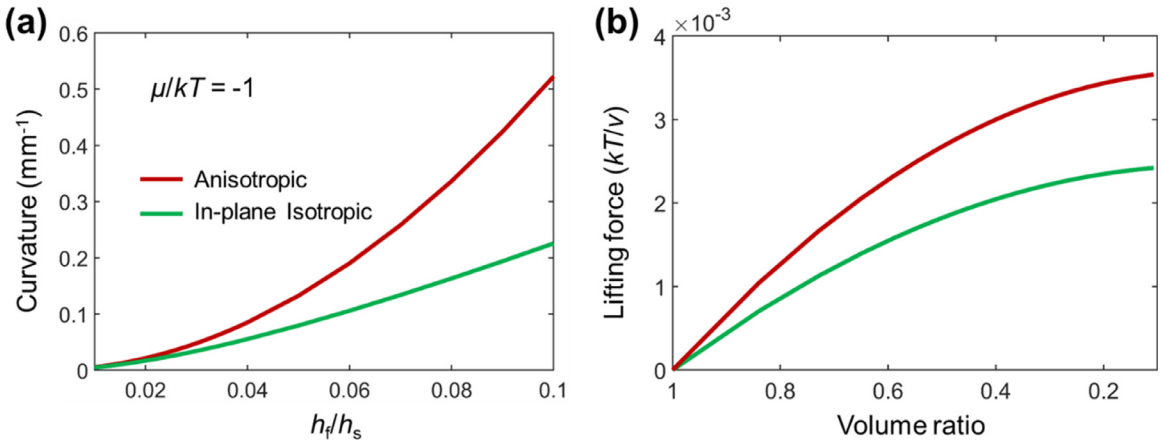

Fig. 16. (a) Bending curvature as a function of thickness ratio h_f/h_s evaluated at $\mu/kT=-1$. (b) Lifting force of the WG/PI actuator as a function of volume ratios for anisotropic WG active layer and in-plane isotropic WG active layer.

water content has been depleted. The final curvature is evaluated at $\mu/kT=-1$. The dependence of the bending curvature on h_f/h_s is also shown in Fig. 16a, for both aligned CNF and randomly distributed CNF actuators.

We also calculate the lifting force by clamping the WG/PI bilayer stripe in the axial direction. The lifting force is the reaction force induced over the two ends where the fixed boundary condition is applied. Fig. 16b plots the lifting forces as a function of the volume ratio. It can be concluded that the anisotropic actuator has a lifting capacity approximately 1.5 times higher than the actuator with randomly distributed fibers.

5. Conclusion

From the perspective of micromechanics, we establish a physics-based constitutive model suitable for microfiber-reinforced anisotropic hydrogels. The hydrogel/microfiber material system can be described by a thermodynamics free energy composed of three terms: the strain energy related to the polymer network deformation, the mixing energy due to the water association with hydrophilic polymer chains, in addition to the free energy stemming from the strained microfibers. We adopt the Fung-type elastic model to capture the nonlinear behavior of cellulose microfibers in wood-based hydrogels. The proposed constitutive model accounts for three-dimensional directional distributions of microfibers, enabling the investigation of hydrogels with arbitrary fiber configurations. For three different types of microfiber configurations, namely, the perfectly aligned microfibers, microfibers uniformly distributed in a plane, and microfibers following in-plane von Mises distribution, we examine the anisotropic mechanical behaviors of the μFRGs in terms of free swelling/dehydration and uniaxial tension. Theoretical predictions of the stress-strain behaviors of PAM hydrogels reinforced by cellulose fibers agree well with experimental results. Moreover, we demonstrate the proposed constitutive law is suitable for wood-based hydrogels, an aggregate of nanocellulose network and water molecules, reinforced by micro-sized cellulose bundles. The constitutive model is applied to the wood-based hydrogel to evaluate and compare the actuation performance of WG/PI bilayer actuators with anisotropic and in-plane isotropic WG layer. We expect the proposed model to deliver insight into the deformation mechanics of microfiber reinforced anisotropic hydrogels such as wood-based hydrogels and promote the development of this novel type of anisotropic soft materials towards soft machines with enhanced functional applications.

Declaration of Competing Interest

We would like to confirm that we have no known competing financial interestes or personal relationships that could influence the work reported in this paper.

CRediT authorship contribution statement

Jian Cheng: Methodology, Investigation, Writing - original draft. **Zheng Jia:** Conceptualization, Methodology, Investigation, Writing - review & editing. **Teng Li:** Conceptualization, Supervision, Resources, Methodology, Writing - review & editing.

Acknowledgements

Teng Li and Jian Cheng acknowledge the support of NASA (Grant number: NNX12AM02G). Zheng Jia acknowledges the financial support from the National Natural Science Foundation of China (No. 11802269), the One-hundred Talents Program of Zhejiang University, and also the Fundamental Research Funds for the Central Universities in China.

Appendix A. The modified Fung-Type model

To simulate the effective stress-strain law of biological fibers, such as collagen fibers, that cannot support compression, the simplest approach is to modify the Fung-type model by setting $S_{\text{fiber}} = 0$ for $\lambda^{\text{f}} < 1$, where $\lambda^{\text{f}} = \sqrt{\boldsymbol{N}\cdot\boldsymbol{C}\boldsymbol{N}} = \sqrt{I_4}$ is the fiber stretch. Note that I_4 is the pseudo-invariants of $\boldsymbol{C}$ and $\boldsymbol{N}\otimes\boldsymbol{N}$ (Holzapfel, 2000). The fiber stress-strain relationship thus takes the form that

$$S_{\text{fiber}} = \begin{cases} 0, & if\ \lambda^{\text{f}} < 1 \\ \dfrac{E}{B}\left[e^{B(\lambda^{\text{f}}-1)} - 1\right], & if\ \lambda^{\text{f}} \geq 1 \end{cases} \tag{A1}$$

The modified Fung-type model can be incorporated into the theoretical framework developed in this work to investigate the deformation of anisotropic hydrogel reinforced by collagen fibers. All equations of state can be solved numerically via Newton-Raphson method.

Appendix B. Mechanical behavior of anisotropic hydrogels with fixed water content

The wood-based hydrogel reported by Kong et al. (Kong et al., 2018) does not exchange water with the environment, such that the water content and the volume of the gel are conserved. To model its stress-strain behavior and compare the theoretical predictions to the experimental results, we modify the free energy in Eq. (13) by fixing the volume ratio J, i.e.,

$$W(\mathbf{F}) = \frac{NkT}{2\Lambda_0^3}\left[I_1\Lambda_0^2 - 3\right] + \int_0^{2\pi}\int_0^{\pi} U_{\text{fiber}}(\mathbf{F}|\boldsymbol{N})\rho(\theta,\phi)\sin\phi d\phi d\theta + D \tag{B1}$$

where $D = -\frac{NkT}{\Lambda_0^3}\log(J\Lambda_0^3) - \frac{kT}{\nu\Lambda_0^3}[(J\Lambda_0^3 - 1)\log(\frac{J\Lambda_0^3}{J\Lambda_0^3 - 1}) + \frac{\chi}{J\Lambda_0^3} + \frac{\mu}{kT}(J\Lambda_0^3 - 1)]$ is a constant. As mentioned above, the volume ratio $J = det(\mathbf{F})$ is fixed. To enforce this constraint, we add the free-energy function $W(\mathbf{F})$ a term $p[J - det(\mathbf{F})]$, where p is a Lagrange multiplier. Then the principal nominal stress in the μFRG can be obtained as

$$\frac{S_i}{kT/\nu} = \frac{N\nu}{\Lambda_0}\lambda_i - \frac{p}{\lambda_i} + \frac{\nu}{kT}\int_0^{2\pi}\int_0^{\pi}\frac{\partial U_{\text{fiber}}}{\partial\lambda^{\text{f}}}\frac{\partial\lambda^{\text{f}}}{\partial\lambda_i}\rho(\theta,\phi)\sin\phi d\phi d\theta \tag{B2}$$

where $i = 1, 2, 3$. For the cellulose-fiber-reinforced PAM hydrogel reported by Kong et al., all fibers are aligned along the longitudinal direction of the gel, which is defined as the x_1 direction here. By adopting a Fung-type fiber model given in Eq. (17), the uniaxial stress-strain behavior is given by

$$S_i = \frac{NkT}{\Lambda_0}\left(\lambda - \lambda^{-2}\right) + \frac{E}{B}\left[e^{B(\lambda-1)} - 1\right] \tag{B3}$$

where $\lambda - 1$ gives the engineering strain. Eq. (B3) is used to plot the stress-strain curve of cellulose-fiber-reinforced PAM hydrogel shown in Fig. 6a and 6b.

References

Ahmed, E.M., 2015. Hydrogel: preparation, characterization, and applications: a review. J. Adv. Res. 6, 105–121.
Astruc, L., Morch, A., Witz, J.F., Novacek, V., Turquier, F., Hoc, T., Brieu, M., 2019. An anisotropic micro-ellipsoid constitutive model based on a microstructural description of fibrous soft tissues. J. Mech. Phys. Solids 131, 56–73.
Billiet, T., Vandenhaute, M., Schelfhout, J., Van Vlierberghe, S., Dubruel, P., 2012. A review of trends and limitations in hydrogel-rapid prototyping for tissue engineering. Biomaterials 33, 6020–6041.
Bosnjak, N., Wang, S., Han, D., Lee, H., Chester, S.A., 2019. Modeling of fiber-reinforced polymeric gels. Mech. Res. Commun. 96, 7–18.
Burgert, I., Fratzl, P., 2009. Plants control the properties and actuation of their organs through the orientation of cellulose fibrils in their cell walls. Integr. Comp. Biol. 49, 69–79.
Cabello, M., Zurbitu, J., Renart, J., Turon, A., Martinez, F., 2016. A non-linear hyperelastic foundation beam theory model for double cantilever beam tests with thick flexible adhesive. Int. J. Solids. Struct. 80, 19–27.
Calvert, P., 2009. Hydrogels for soft machines. Adv. Mater. 21, 743–756.
Chen, S., Schueneman, G., Pipes, R.B., Youngblood, J., Moon, R.J., 2014. Effects of crystal orientation on cellulose nanocrystals-cellulose acetate nanocomposite fibers prepared by dry spinning. Biomacromolecules 15, 3827–3835.
Compton, B.G., Lewis, J.A., 2014. 3D-Printing of lightweight cellular composites. Adv. Mater. 26, 5930–5935.
De France, K.J., Xu, F., Hoare, T., 2018. Structured macroporous hydrogels: progress, challenges, and opportunities. Adv Healthc Mater 7, 1700927.
Flory, P.J., Rehner, J., 1943. Statistical mechanics of cross-linked polymer networks I rubberlike elasticity. J. Chem. Phys. 11, 512–520.
Fratzl, P., Elbaum, R., Burgert, I., 2008. Cellulose fibrils direct plant organ movements. Faraday Discuss. 139, 275–282.
Fung, Y.C.B., 1967. Elasticity of soft tissues in simple elongation. Am. J.Physiol. 213, 1532–1544.
Gladman, A.S., Matsumoto, E.A., Nuzzo, R.G., Mahadevan, L., Lewis, J.A., 2016. Biomimetic 4D printing. Nat. Mater. 15, 413–419.
Holzapfel, G.A., 2000. Nonlinear Solid Mechanics: A Continuum Approach for Engineering. Wiley.
Holzapfel, G.A., Ogden, R.W., 2015. On the tension-compression switch in soft fibrous solids. Eur. J. Mech. a-Solids 49, 561–569.
Hong, W., Liu, Z., Suo, Z., 2009. Inhomogeneous swelling of a gel in equilibrium with a solvent and mechanical load. Int. J. Solids. Struct. 46, 3282–3289.
Hong, W., Zhao, X., Suo, Z., 2010. Large deformation and electrochemistry of polyelectrolyte gels. J. Mech. Phys. Solids 58, 558–577.
Hong, W., Zhao, X., Zhou, J., Suo, Z., 2008. A theory of coupled diffusion and large deformation in polymeric gels. J. Mech. Phys. Solids 56, 1779–1793.
Ionov, L., 2014. Hydrogel-based actuators: possibilities and limitations. Materials Today 17, 494–503.
Kanner, L.M., Horgan, C.O., 2008. Plane strain bending of strain-stiffening rubber-like rectangular beams. Int. J. Solids. Struct. 45, 1713–1729.
Kim, Y.S., Liu, M., Ishida, Y., Ebina, Y., Osada, M., Sasaki, T., Hikima, T., Takata, M., Aida, T., 2015. Thermoresponsive actuation enabled by permittivity switching in an electrostatically anisotropic hydrogel. Nat. Mater. 14, 1002–1007.

Kokkinis, D., Schaffner, M., Studart, A.R., 2015. Multimaterial magnetically assisted 3D printing of composite materials. Nat. Commun. 6, 8643.
Kong, W., Wang, C., Jia, C., Kuang, Y., Pastel, G., Chen, C., Chen, G., He, S., Huang, H., Zhang, J., Wang, S., Hu, L., 2018. Muscle-Inspired highly anisotropic, strong, Ion-Conductive Hydrogels. Adv. Mater. 30, 1801934.
Kuang, Y., Chen, C., Cheng, J., Pastel, G., Li, T., Song, J., Jiang, F., Li, Y., Zhang, Y., Jang, S.H., Chen, G., Li, T., Hu, L., 2019. Selectively aligned cellulose nanofibers towards high-performance soft actuators. Extreme Mech. Lett. 29, 100463.
Lian, J., Sharaf, M., Archie, F., Muenstermann, S., 2013. A hybrid approach for modelling of plasticity and failure behaviour of advanced high-strength steel sheets. Int. J. Damage Mech. 22, 188–218.
Lin, P., Zhang, T., Wang, X., Yu, B., Zhou, F., 2016. Freezing molecular orientation under stretch for high mechanical strength but anisotropic hydrogels. Small 12, 4386–4392.
Liu, M., Ishida, Y., Ebina, Y., Sasaki, T., Hikima, T., Takata, M., Aida, T., 2015a. An anisotropic hydrogel with electrostatic repulsion between cofacially aligned nanosheets. Nature 517, 68–72.
Liu, S., Stupp, S.I., de la Cruz, M.O., 2018. Anisotropic contraction of fiber-reinforced hydrogels. Soft Matter 14, 7731–7739.
Liu, T., Huang, M., Li, X., Wang, C., Gui, C.X., Yu, Z.Z., 2016a. Highly compressible anisotropic graphene aerogels fabricated by directional freezing for efficient absorption of organic liquids. Carbon N Y 100, 456–464.
Liu, Y., Zhang, H., Wang, J., Zheng, Y., 2016b. Anisotropic swelling in fiber-reinforced hydrogels: an incremental finite element method and its applications in design of bilayer structures. Int. J. Appl. Mech. 8, 1640003.
Liu, Y., Zhang, H., Zhang, J., Zheng, Y., 2015b. Constitutive modeling for polymer hydrogels: a new perspective and applications to anisotropic hydrogels in free swelling. Eur. J. Mech. a-Solids 54, 171–186.
Lu, T., Chen, Z., Qi, H.J., Wang, T.J., 2018. A micro-structure based constitutive model for anisotropic stress-strain behaviors of artery tissues. Int. J. Solids. Struct. 139, 55–64.
Markstedt, K., Mantas, A., Tournier, I., Avila, H.M., Hagg, D., Gatenholm, P., 2015. 3D Bioprinting human chondrocytes with nanocellulose-alginate bioink for cartilage tissue engineering applications. Biomacromolecules 16, 1489–1496.
Mredha, M.T.I., Guo, Y.Z., Nonoyama, T., Nakajima, T., Kurokawa, T., Gong, J.P., 2018. A facile method to fabricate anisotropic hydrogels with perfectly aligned hierarchical fibrous structures. Adv. Mater. 30, 1704937.
Nardinocchi, P., Pezzulla, M., Teresi, L., 2015. Steady and transient analysis of anisotropic swelling in fibered gels. J. Appl. Phys. 118, 244904.
Omidinia-Anarkoli, A., Boesveld, S., Tuvshindorj, U., Rose, J.C., Haraszti, T., De Laporte, L., 2017. An injectable hybrid hydrogel with oriented short fibers induces unidirectional growth of functional nerve cells. Small 13, 1702207.
Palagi, S., Mark, A.G., Reigh, S.Y., Melde, K., Qiu, T., Zeng, H., Parmeggiani, C., Martella, D., Sanchez-Castillo, A., Kapernaum, N., Giesselmann, F., Wiersma, D.S., Lauga, E., Fischer, P., 2016. Structured light enables biomimetic swimming and versatile locomotion of photoresponsive soft microrobots. Nat. Mater. 15, 647–653.
Pan, Y., Zhong, Z., 2014. A nonlinear constitutive model of unidirectional natural fiber reinforced composites considering moisture absorption. J. Mech. Phys. Solids 69, 132–142.
Sano, K., Ishida, Y., Aida, T., 2018. Synthesis of anisotropic hydrogels and their applications. Angewandte Chemie-International Edition 57, 2532–2543.
Siqueira, G., Kokkinis, D., Libanori, R., Hausmann, M.K., Gladman, A.S., Neels, A., Tingaut, P., Zimmermann, T., Lewis, J.A., Studart, A.R., 2017. Cellulose nanocrystal inks for 3D printing of textured cellular architectures. Adv. Funct. Mater. 27, 1604619.
Timoshenko, S., 1925. Analysis of bi-metal thermostats. J. Opt. Soc. Am. Rev. Sci. Instrum. 11, 233–255.
Tonge, T.K., Voo, L.M., Nguyen, T.D., 2013. Full-field bulge test for planar anisotropic tissues: part II - A thin shell method for determining material parameters and comparison of two distributed fiber modeling approaches. Acta. Biomater. 9, 5926–5942.
Torres-Rendon, J.G., Femmer, T., De Laporte, L., Tigges, T., Rahimi, K., Gremse, F., Zafarnia, S., Lederle, W., Ifuku, S., Wessling, M., Hardy, J.G., Walther, A., 2015. Bioactive gyroid scaffolds formed by sacrificial templating of nanocellulose and nanochitin hydrogels as instructive platforms for biomimetic tissue engineering. Adv. Mater. 27, 2989–2995.
Tsai, H., Pence, T.J., Kirkinis, E., 2004. Swelling induced finite strain flexure in a rectangular block of an isotropic elastic material. J. Elast. 75, 69–89.
Tseng, H., Puperi, D.S., Kim, E.J., Ayoub, S., Shah, J.V., Cuchiara, M.L., West, J.L., Grande-Allen, K.J., 2014. Anisotropic poly(ethylene glycol)/polycaprolactone hydrogel-fiber composites for heart valve tissue engineering. Tissue Eng. Part A 20, 2634–2645.
Wang, B., Benitez, A.J., Lossada, F., Merindol, R., Walther, A., 2016. Bioinspired mechanical gradients in cellulose nanofibril/polymer nanopapers. Angewandte Chemie-International Edition 55, 5966–5970.
Xiao, R., 2016. Modeling mismatch strain induced self-folding of bilayer gel structures. Int. J. Appl. Mech. 8, 1640004.
Xiao, R., Gou, X., Chen, W., 2016. Suppression of electromechanical instability in fiber-reinforced dielectric elastomers. AIP Adv. 6, 035321.
Ye, D., Yang, P., Lei, X., Zhang, D., Li, L., Chang, C., Sun, P., Zhang, L., 2018. Robust anisotropic cellulose hydrogels fabricated via strong self-aggregation forces for cardiomyocytes unidirectional growth. Chem. Mater. 30, 5175–5183.
Zhou, Y., Hu, J., Liu, Z., 2019. Deformation behavior of fiber-reinforced hydrogel structures. Int. J. Struc. Stab. Dynam. 19, 1950032.